RHODES UNIVERSITY

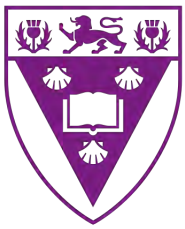

RHODES UNIVERSITY

Where leaders learn

MeerKAT observations of the Abell 141 galaxy cluster

by

Savannah Mae Stanbury

Submitted in fulfilment of the

academic requirements for the degree of

Masters

in

Physics

Rhodes University, Makhanda

Supervised by Prof. O. M. Smirnov & Prof. G. Bernardi

February 16, 2024

Declaration of Non-Plagiarism

I, **Savannah Stanbury** declare that

1. The research reported in this thesis, except where otherwise indicated, is my original research.
2. This thesis has not been submitted for any degree or examination at any other university.
3. This thesis does not contain other persons' data, pictures, graphs or other information, unless specifically acknowledged as being sourced from other persons.
4. This thesis does not contain other persons' writing, unless specifically acknowledged as being sourced from other researchers.

Abstract

Galaxy clusters are the largest gravitationally bound structures in the universe, hosting a hot, tenuous gas that permeates their volume, known as the intracluster medium. A fraction of the intracluster medium is composed of relativistic electrons that, when accelerated in magnetic fields, radiate synchrotron emission. Synchrotron emission occurs on scales ranging between individual galaxies to $\sim$Mpc scales and beyond, with a few examples of radio emission observed on a few Mpc scales, "bridging" between cluster pairs. A possible third system to host radio emission on such large scales is the Abell 141 cluster, a system composed of two subclusters, where its X-ray emission has been seen in the connecting region. Radio observations at 150 MHz and 943 MHz detected diffuse emission from the two systems, although the limited angular resolution prevented a detailed picture of the system.

In this thesis, we present observations at 1.28 GHz of the A 141 system, taken with the MeerKAT telescope, with the aim of further characterising its diffuse radio emission. We obtain an image with a $5.1'' \times 4.4''$ angular resolution and an rms noise of 9 μJy beam^{-1} that we use to identify and subtract compact sources. Subsequently, we generate a $19'' \times 17''$ angular resolution

and an rms noise of 8.8 μJy beam^{-1} where we detected diffuse radio emission extending over 0.9 Mpc. We find its integrated flux density to be 10.8 ± 0.3 mJy.

The radio surface brightness peaks at the location of the Northern subcluster, although, it is offset by a few arcmin with respect to the peak of the X-ray emission. The radio morphology extends over both subclusters, and, thanks to the angular resolution of our observations, we can clearly see radio emission in the region between the two subclusters, though it does not closely follow the X-ray morphology.

In this respect, A 141 remains a somewhat unique system. We find tentative evidence for "bridge"-like radio emission at GHz frequency, whereas previous bridges were detected at low frequency only (< 200 MHz), which closely matches the morphology of the X-ray/thermal emission. We confirmed the spectral index of the integrated radio emission to be $\alpha \ -1.06 \ \pm \ 0.09$, which would somewhat disfavour a scenario where particles are accelerated by turbulence in the early merger state, which is, conversely, the preferred explanation for the bridges detected at low frequencies. Further observations at lower frequencies may be able to shed light on the nature of this system.

Acknowledgments

The financial assistance of the South African Radio Astronomy Observatory (SARAO) towards this research is hereby acknowledged (www.sarao.ac.za).

I would like to thank my supervisors, Prof. Oleg Smirnov and Prof. Gianni Bernardi, for being a guiding light throughout this journey, and for their endless support and continued patience. I would also like to thank all the RATT supervisors and fellow RATT students who were always ready to help me whenever and wherever possible.

Additionally, I thank the Rhodes University Physics and Electronics Department for their continued support throughout the years.

Last but not least, I thank my loved ones for their everlasting encouragement and support, and without whom, I would not be where I am today.

List of Figures

1.1 Diagram of Bremsstrahlung Emission 4
1.2 Diagram of Synchrotron Emission 6
1.3 Radio Halo in the Coma Cluster 10
1.4 Mini-Halo in the Perseus Cluster 15
1.5 Radio Bridge in Abell 399- Abell 401 21
1.6 Radio Bridge in Abell 1758 23
1.7 Composite image of Abell 141 26
1.8 Diagram of a MeerKAT Antenna 28

2.1 Schematic of the Double Slit Experiment of Thomas Young 33
2.2 Simplified Diagram of a Two-Dish Interferometer 34
2.3 Diagram of Relationship between u,v-plane and l,m-plane 36
2.4 uv-tracks and uv-coverage of our MeerKAT data 36
2.5 PSF of our MeerKAT Data 38

3.1 Dirty MeerKAT image of Abell 141 52

3.2 Deconvolved MeerKAT image of Abell 141 53
3.3 Self-Calibrated MeerKAT image of Abell 141 54
3.4 Comparison between MeerKAT deconvolved and self-calibrated image of Abell 141 55
3.5 Example of bad gain solutions 56
3.6 Fourier transformed image featuring bad gain solutions 58
3.7 Fianl self-calibrated MeerKAT image of Abell 141 59
3.8 Diffuse emission associated to Abell 141 in the self-calibrated MeerKAT image . 60
3.9 Unifrom weighted restored MeerKAT image of Abell 141 61
3.10 Uniform weighted residual MeerKAT image of Abell 141 62
3.11 Briggs weighted and tapered MeerKAT image of Abell 141 63

4.1 ASKAP image of Abell 141 with MeerKT contours overlaid 65
4.2 XMM-Newton image of Abell 141 with MeerKAT contours overlaid 66
4.3 Uniform weighted MeerKAT of Abell 141 withe labeled, sources that are subtracted 67

List of Acronyms

1 GC First Generation Calibration

2GC Second Generation Calibration

ASKAP Australian Square Kilometre Array Pathfinder

CARACal Containerized Automated Radio Astronomy Calibration

CASA Common Astronomy Software Application

CDM Constant Cold Dark Matter

CMB Cosmic Microwave Background

FAST Five-hundred-meter Aperture Spherical Telescope

GBT Green Bank Telescope

GMRT Giant Metrewave Radio Telescope

ICM IntraCluster Medium

JVLA Janksy Very Large Array

LOFAR Low Frequency Array

MFS Multi Frequency Synthesis

Pan STARRS Panoramic Survey Telescope and Rapid Response System

PSF Point Spread Function

RFI Radio Frequency Interference

RIME Radio Interferometry Measurement Equation

SKA Square Kilometer Array

SZ Sunyaev-Zel'dovich

uGMRT Upgraded Giant Metrewave Radio Telescope

USSRH Ultra Steep Spectrum Radio Halo

WSRT Westerbork Synthesis Radio Telescope

Contents

Declaration of Non Plagiarism i

Declaration of Publications ii

Abstract ii

Acknowlegments iv

1 Introduction 1

1.1 Galaxy Clusters 1

1.1.1 Formation and Evolution 1

1.1.2 The IntraCluster Medium 3

1.2 Multi-wavelength Emission from Galaxy Clusters 7

1.2.1 X-Ray 7

1.2.2 SZ-Effect 8

1.2.3 Radio 8

1.3 Classification of Synchrotron Sources . . . 9
1.3.1 Giant Radio Halos . . . 9
1.3.2 Mini Radio Halos . . . 14
1.3.3 Unification of Mini-Halos and Giant Radio Halos . . . 16
1.3.4 Radio Relics . . . 16
1.3.5 Radio Bridges . . . 18
1.4 A Few Special Cases . . . 19
1.4.1 The Abell 399 - 401 pair . . . 19
1.4.2 Abell 1758 . . . 22
1.4.3 Abell 141 . . . 24
1.4.4 Similarities between galaxy clusters hosting radio bridges . . . 26
1.5 The MeerKAT radio telescope . . . 27
1.6 Thesis Motivation . . . 29

2 Radio Technologies and Techniques **30**
2.1 Single Dish Radio Astronomy . . . 31
2.2 Fourier Transform . . . 31
2.3 Radio interferometry . . . 33
2.4 Radio Interferometry Measurement Equation . . . 41
2.5 First Generation Calibration . . . 43
2.6 Second Generation Calibration . . . 45

3 Observations and Data Reduction **48**
3.1 Observations . . . 48
3.2 Data Reduction . . . 49

4 Results and Discussion **64**
4.1 Comparison with similar systems . . . 70

5 Conclusions **73**

CHAPTER 1

Introduction

Galaxy clusters are made up of hundreds to thousands of galaxies gravitationally bound together. They are the largest virialised objects in the universe and are thus fantastic laboratories for a variety of physical phenomena. As a result, galaxy clusters have been widely studied for the past 30 years and remain to be one of the main areas of research in astronomy and cosmology.

1.1 Galaxy Clusters

1.1.1 Formation and Evolution

A structure formation model is a theoretical model used to describe the construction of large-scale structures within the universe. These large-scale structures include galaxy clusters. The most accurate structure formation model to date is the cosmological constant (Λ) dominated cold dark matter (CDM) model (Molnar, 2016), which has accurately predicted and explained a wide

array of astronomical phenomena, including expansion of the universe (Riess et al., 1998), and measurements of the cosmic microwave background (CMB) (Planck Collaboration et al., 2020).

According to the ΛCDM model, large-scale structures are created through a hierarchical structure formation, meaning that they are formed from the merger of smaller structures, due to gravitational instabilities. Fractional fluctuations of the density of matter results in an eventual collapse, causing the construction of dark matter clumps. Over time, these dark matter clumps merge to form larger clumps, and eventually, large scale structures, such as galaxy clusters. The fluctuation in the density of matter in the ΛCDM model can be described using the overdensity field,

$$\delta(\mathbf{x}) = \left(\rho(\mathbf{x}) - \bar{\rho}_{\mathrm{m}}\right)/\bar{\rho}_{\mathrm{m}} \tag{1.1}$$

where $\bar{\rho}_{\mathrm{m}}$ is the mean mass density of the universe (Kravtsov & Borgani, 2012). The evolution of such fluctuations can be described either by the *linear* or *non-linear* models. In the initial stages of the universe, the linear approximation (where $\delta(\mathbf{x}) \ll 1$) allowed the density fluctuations to be small and proportional to the scale factor of the universe. When the linear approximation breaks down, the non-linear approximation (where $\delta(\mathbf{x}) \gg 1$) results in larger, non-linear, fluctuations in density, where numerical simulations are required to fully grasp the evolution of large-scale structures (Kravtsov & Borgani, 2012).

The interaction of gravity with dark matter and dark energy in the early universe resulted in a structure that consists of interconnected filaments of density. At the intersection of these thread-like filaments are dense areas of cosmic matter, such as stars and galaxies, which form as nodes in between the filamentary structures. This structure is known as the *cosmic web.* (Molnar, 2016).

Galaxy clusters form at the nodes of the cosmic web, through highley energetic *merger events*. which can release energies up to 10^{64} ergs on a timescale of a few Gyr (Van Weeren et al., 2019). Depending on their merging state, galaxy clusters can be classified as either *relaxed*, undisturbed systems or *merging*, disturbed systems (Van Weeren et al., 2019). Disturbed

systems can be further classified as *pre-merging* or *merging*. Galaxy clusters in a pre-merger phase are defined to be gravitationally bound but not yet interacting. Multiple methods have been identified to determine the dynamical activity of galaxy clusters, including examining their X-ray morphologies (Kravtsov & Borgani, 2012), as disturbed clusters will often show evidence of a disturbed X-ray morphology (Parekh et al., 2015).

1.1.2 The IntraCluster Medium

The composition of a galaxy cluster's baryoninc mass is as follows: around $\sim$ 5% is galaxies, $\sim$ 80% is dark matter, and the remaining $\sim 15\%$ comprises of the *intracluster medium* (ICM). The ICM which is a hot (10^7 –10^8 K), dilute (10^{-3} particles cm^{-3}), ionized gas, consisting of relativistic particles and magnetic fields. It permeates the volume of the galaxy cluster, and is held in place by the gravitational pull of the cluster (Feretti et al., 2012; Van Weeren et al., 2019). As the ICM makes up a large percentage of galaxy clusters, studying the ICM can reveal essential properties of the galaxy cluster. The ICM is observed at X-ray wavelengths, as it emits thermal bremsstrahlung radiation. Over the past few decades, relativistic particles present in the ICM have been detected through non-thermal synchrotron emissions, visible in the radio regime (e.g. Brunetti, 2004).

Bremmstrahlung Emission

The ICM emits thermal *bremsstrahlung emission* (Brunetti, 2004; Van Weeren et al., 2019). Bremsstrahlung emission, also known as free-free emission, or braking emission, is a mechanism that produces thermal emission, visible in the X-rays regime. The temperature and density of the predominantly hydrogen-based ICM allows for gas to be emitted via bremsstrahlung emission (Sarazin, 1986); the emission occurs due to a collision between a high-energy (keV) electron from the ICM and ions with electric fields strong enough to decelerate the electron (Forman & Jones, 1982). This process can be seen in Figure 1.1. The X-ray emission produced is useful for studying the gravitational potential of the cluster which is occupied by the ICM.

Relativistic electrons and protons in the ICM may also result in non-thermal X-ray emission

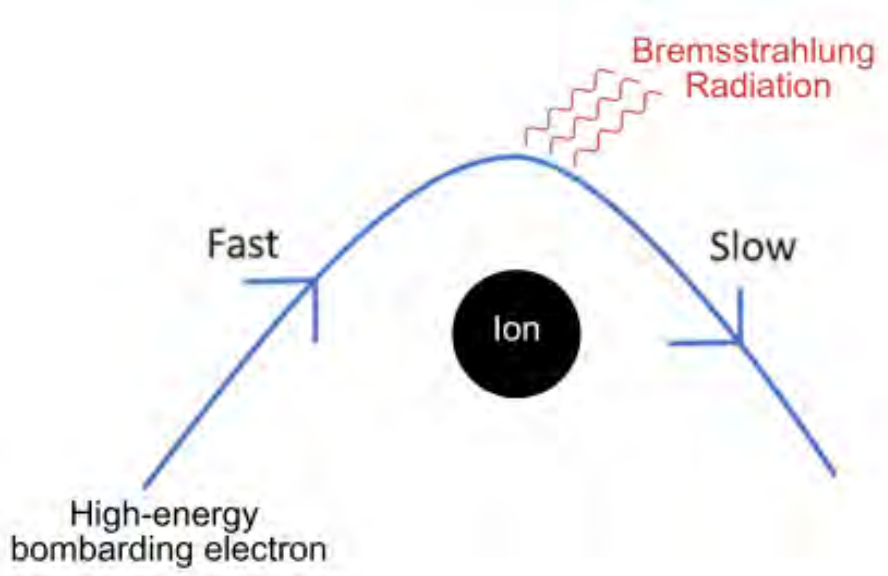

Figure 1.1: A diagram explaining bremsstrahlung emission (Image adapted from https://www.radiologycafe.com/frcr-physics-notes/X-ray-imaging/production-of-X-rays/). The bombarding electron is decelerated due to the electric field of the ion, and bremsstrahlung radiation is emitted.

in the form of Inverse Compton (IC) scattering (Brunetti, 2004).

Recent studies of the ICM in the radio regime, however, reveal a non-thermal component in the form of relativistic electrons and magnetic fields. These relativistic electrons emit *synchrotron emission*.

Synchrotron Emission

Energised, relativistic electrons with a Lorenz factor of $\gamma > 10^3$ in the presence of μGauss magnetic field lines in the ICM spiral in the magnetic field, causing non-thermal radiation in the form of synchrotron emission (Van Weeren et al., 2019). A diagram of this mechanism can be seen in Figure 1.2.

The synchrotron radiation occurs over large scales (Duchesne et al., 2021), and is observable at radio, optical, and X-ray wavelengths. The average power radiated over all angles between the electron velocity and magnetic field lines, $\langle P \rangle$, depends on the energy of the electrons and the strength of the magnetic field lines, as in Condon & Ransom (2016),

$$\langle P \rangle \propto E^2 B^2. \tag{1.2}$$

Electron particles emitting synchrotron emission will lose energy depending on their frequencies, with higher energy loss occurring at higher frequencies. After a period of time, the particles are no longer relativistic due to their loss of energy; these particles will no longer emit synchrotron radiation. The time period over which this loss occurs is known as the *synchrotron age*. Galaxy clusters exhibit synchrotron ages of $t_{age} \lesssim 10^8$ years (Van Weeren et al., 2019).

However, many sources older than this still emit synchrotron radiation, indicating that the particles must be somehow re-accelerated. Currently, there are several proposed *re-acceleration mechanisms.*

It is widely believed that during highly energetic (10^{64} ergs, over a timescale of a few Gyr (Van Weeren et al., 2019)) merger events occuring between galaxies, a fraction of energy released by such events is dissipated into the ICM, via *shocks*.

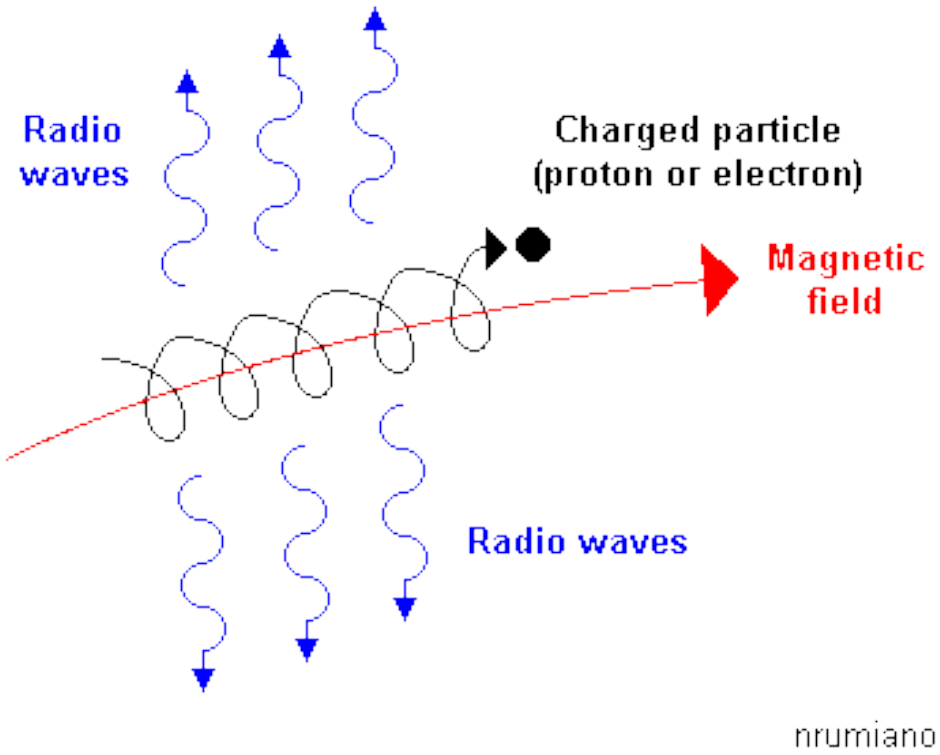

Figure 1.2: A diagram explaining synchrotron emission. The charged particle spirals around the magnetic field lines, emitting radio waves in the form of synchrotron radiation (figure taken from https://lightandcolourinmoderntechnology.weebly.com/synchrotron-radiation.html)

A shock is an energy wave, defined as having a Mach number $\gg 1$. That is, the speed of the flow of electrons is significantly greater than that of the speed of sound in space. Shocks have the ability to compress their surrounding medium; the increase in pressure combined with the constant volume will result in an increase in energy (Hoeft & Brüggen, 2007).

Energy from the shocks, in combination with turbulence from merger events, results in the heating of the ICM (Van Weeren et al., 2019), which subsequently re-accelerates relativistic particles and amplifies magnetic fields. This is done through a series of mechanisms that essentially transfer Mpc scale energy to small scale energy via weak shocks and turbulence (Brunetti & Vazza, 2020). The precise physics of the re-acceleration is poorly understood (Botteon et al., 2018).

Energy is subsequently transferred to various thermal and non-thermal radiation processes, which are visible in the X-ray and radio regime (Duchesne et al., 2021). By studying this emission, particularly that of the ICM, we are able to learn more about reacceleration mechanisms.

1.2 Multi-wavelength Emission from Galaxy Clusters

Galaxy clusters are detectable at several wavelengths, through the emission from the ICM.

1.2.1 X-Ray

X-rays are emitted at the frequency of $10^{17} - 10^{19}$ Hz. The dominant mechanism for X-ray emission from the ICM is thermal brehamslung emission. Galaxy clusters attract matter from the universe, largely due to their size. Their strong potential well causes the attracted matter to collapse to the center of the galaxy cluster, causing collision between particles, which in turn causes bremsstrahlung emission. This emission can be observed with X-ray space telescopes, as X-rays are absorbed by the Earth's atmosphere and need to be observed from beyond the atmosphere. Two examples of X-ray telescopes are National Aeronautic and Space Administration (NASA)'s *Chandra* and the European Space Agency (ESA)'s *X-ray Multi-Mirror Mission* (XMM-Newton)

telescopes.

Sources with high amounts of X-ray emission, such as galaxy clusters, can be characterised by their *X-ray luminosity*, L_X, which is a measure of the X-ray energy emitted per second in the 2-10 keV band. Galaxy clusters have been found to have X-ray luminosities of $\mathrm{L}_X \sim 10^{43} - 10^{45}$ erg s^{-1} (Sarazin, 1986).

X-ray observations are often critical in the studies of galaxy clusters, as the X-ray morphology can provide information on the dynamic state of the galaxy cluster, determining whether it is relaxed or disturbed. This can indicate the merger state of a galaxy cluster. This allows for X-ray observation to probe the hierarchal structure of cluster formation.

1.2.2 SZ-Effect

Sunyaev-Zel'dovich (SZ) emission occurs when the cosmic microwave background (CMB) scatters the high-energy, thermal ICM electrons, through inverse Compton scattering, and causes a distortion of the CMB spectrum, which is independent of redshift. As such, the SZ effect can be used to study galaxy clusters at higher redshifts, where X-ray surface brightness suffers from cosmological dimming caused by the distance between the X-ray emitting sources, and the observer (Van Weeren et al. (2019); Sunyaev & Zeldovich (1970)).

The measured SZ signal can be scaled with X-ray emission to derive the mass of galaxy clusters. Ade et al. (2016) studied a large sample of relaxed and disturbed galaxy clusters with a redshift up to $\mathrm{z} \sim 1.5$, deriving the masses of several well-known galaxy clusters using the SZ signal; this will be referred to as an SZ-derived mass.

1.2.3 Radio

The dominant mechanism for radio emission from galaxy clusters is synchrotron emission. Synchrotron sources are faint, due to their low surface brightness. The surface brightness of a source is described by their flux density, S_ν, in units of *Jansky*, Jy, where 1 Jy = $10^{26}\mathrm{W\ m^{-2}Hz^{-1}}$. Flux

density has a power-law dependency of frequency, ν, as,

$$S_\nu \propto \nu^\alpha \tag{1.3}$$

where α is the spectral index (Brunetti & Jones, 2014). The spectral index indicates how the intensity of the radio waves emitted by a source varies with frequency. Synchrotron sources usually have steep spectral indices, where $\alpha \lesssim -1$, indicating that the sources are brighter at lower frequencies (Van Weeren et al. (2019), Duchesne et al. (2021)). The spectral index is usually calculated by finding the slope (α) of a plot that fits the flux density of a source across several frequencies to a power-law in a log-log space. The faint surface brightness is what has made detection of synchrotron sources somewhat rare until recently, with the production of more sensitive radio telescopes, which are further discussed in detail in Chapter 2. Synchrotron sources can be classified into several subgroups, discusses in the the next section.

1.3 Classification of Synchrotron Sources

Diffuse radio emission is emitted from synchrotron sources that are associated with the ICM. It is currently believed that synchrotron sources are formed as a result of energy that is dissipated into the ICM by shocks and turbulence. While the exact mechanism of particle reacceleration is still largely unknown, what has become clear is that there is a connection between cluster mergers and the formation of synchrotron sources (Botteon et al., 2018). These novel mechanisms can be probed by studying cluster-wide radio sources, such as radio halos, and radio relics.

Diffuse radio emission is commonly divided into subclasses. In this section, we will discuss common synchrotron sources, *radio halos*, *mini-halos*, *radio relics*, and *radio bridges*.

1.3.1 Giant Radio Halos

Giant radio halos are large (typically 1 Mpc - 2 Mpc) extended diffuse emission sources located centrally in merging (disturbed) galaxy clusters (Duchesne et al., 2021). Radio halos roughly trace the brightness distribution of the ICM. The prototypical radio halo, the Coma Cluster

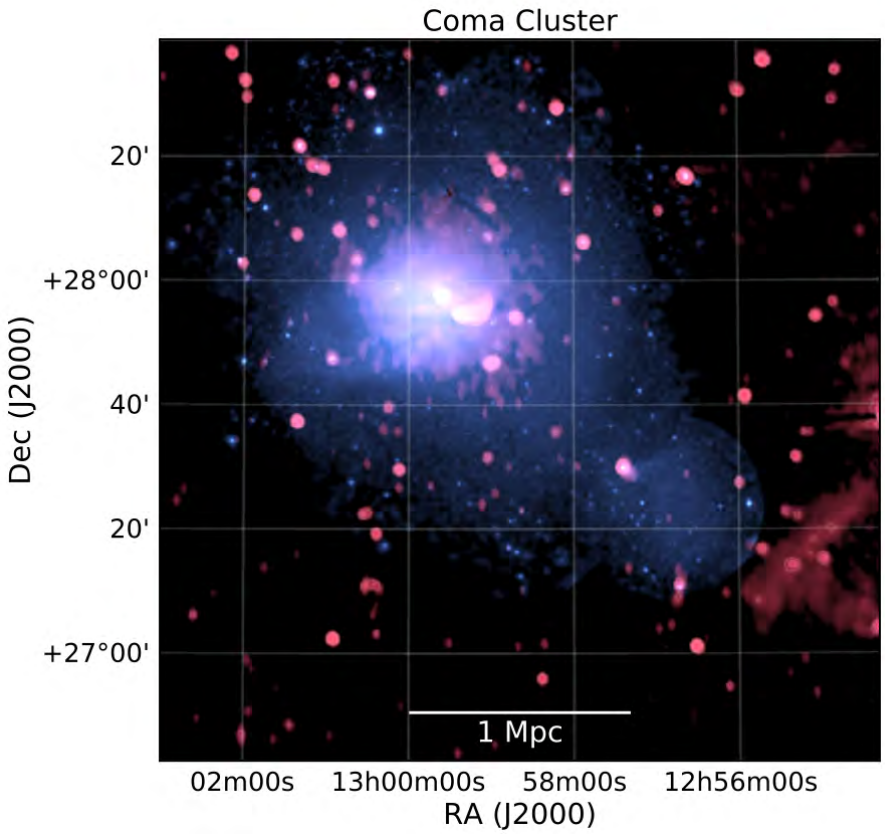

Figure 1.3: The Coma cluster, as imaged by Westerbork Synthesis Radio Telescope (WSRT) radio emission at 352 MHz is shown in red, and XMM-Newton X-ray data taken at 0.4–1.3 keV is shown in blue. This cluster shows the coincidence of radio emission and X-ray emission that is common for radio halos.

(Brown & Rudnick, 2011) is pictured in Figure 1.3

Morphology

The morphology of giant radio halos is typically smooth and regular, while their radiation approximately traces the brightness distribution of the thermal ICM. Radio halos have been shown to have a point-to-point correlation between X-ray and radio brightness distributions (Van Weeren et al., 2019).

Origins of Radio Halos

Given the Mpc size of radio halos, the relatively short radiation time of the radio-emitting electrons implies that the relativistic electrons should be continuously reaccelerated *in situ*. There are two possible mechanisms for this particle acceleration: the *hadronic model* and the *turbulent re-acceleration model.*

In the hadronic model, protons from cosmic rays and the ICM have hadronic interactions, which emit radio emission. The hadronic model is disfavoured due to γ-ray interactions observed in the popular Coma cluster that directly determined that radio halos can not be formed via the hadronic model (Van Weeren et al., 2019; Cassano & Brunetti, 2005). Due to this, giant radio halos are currently believed to form from the turbulent re-acceleration of primary or secondary (seed) electrons through turbulence. This is known as *Fermi II acceleration*.

Fermi II acceleration is a stochastic, turbulence-induced reacceleration mechanism. Turbulence is a process that can inject energy into a medium due to chaotic motions. In the case of radio halos, or large-scale structures, this turbulence is believed to come from a dynamic event, such as a merger, where gravitational energy is converted into turbulence. Through the injection of energy and amplification of magnetic fields, the inhomogeneities of the magnetic field will scatter electrons randomly. The particles thus experience both head-on and overtaking collisions; such collisions result in a gain or loss of energy, respectively. Head-on collisions have a higher probability of occurring; thus, energy, on average, is gained, resulting in the re-acceleration of particles (Rieger et al., 2007; Van Weeren et al., 2019).

However, the origin of the seed electrons is unknown (Botteon et al., 2018). There are currently three widely accepted possibilities of their origin. The first is that the seed electrons are the secondary electrons from proton-proton interaction; the second is previously shock-accelerated particles due to merger events; third, the seed electrons are a result of galaxy outflows from active galactic nuclei (Van Weeren et al., 2019). The seed electrons are then reaccelerated by a fraction of the energy released during a cluster merger event; they begin to emit synchrotron emission at radio frequencies. They are thought to trace the regions in which turbulent relativistic particles

are reaccelerated through scattering via Fermi II mechanism.

Radio halos are expected to be more prominent in massive galaxy clusters undergoing mergers. Cuciti et al. (2021) found that in a study of 75 mass-selected galaxy clusters, separated into high mass ($M \gtrsim 8 \times 10^{14}\ M_{\odot}$) and low mass ($M < 8 \times 10^{14}\ M_{\odot}$) bins, the number of galaxies hosting a radio halo fell from $\sim 70\%$ in the high-mass group, to $\sim 35\%$ in the low mass group. Additionally, they found that $\sim 90\%$ of the radio halo-hosting galaxy clusters were undergoing a merger.

In a study of 205 galaxy clusters, Giovannini et al. (1999) found that $\sim 30\%$ of galaxy clusters at a redshift of $z \leq 0.2$ with a corresponding X-ray luminosity ($L_X > 1.0 \times 10^{45}$ ergs s^{-1}) hosted radio halos, while Giovannini et al. (2020) found that $\sim 70\%$ galaxy clusters at a redshift of $z = 0.3 - 0.6$ with X-ray luminosity hosted radio halos. This is indicative of correlations between the power of radio halos and X-ray luminosity; radio halos are more likely to form in galaxy clusters with high X-ray luminosity.

Current re-acceleration models predict that a large fraction of giant radio halos, with a mass of $M_{500} \approx 4 - 7 \times 10^{14} M_{\odot}$ and $z \approx 0.1 - 0.3$ should have steep spectral indices ($\alpha <$ -1.5, where $S_{\nu} \propto \nu^{\alpha}$) caused by losses due to strong synchrotron radiation, as well as inverse Compton losses (Di Gennaro et al., 2021). Despite this, very few radio halos have been detected with steep spectral indices; hence detecting such steep spectral indices is critical for testing the current model.

Radio Spectra

Determining the spectral properties of radio halos is a crucial step in understanding their origin. However, it can be troublesome to make reliable flux density measurements when a halo has a low signal-to-noise, as is often the case with extended sources. As a result, the uncertainties in the radio spectra measurements are carefully calculated as in Cassano et al. (2013),

$$\sigma_{f_H} = \sqrt{(\delta_{\text{cal}}\, f_H)^2 + \left(\text{rms}\,\sqrt{N_{\text{beam}}}\right)^2} \tag{1.4}$$

where the first term takes into account the assumption that the map noise of the halo has a Gaussian distribution; the second term accounts for the uncertainty in the flux-scale, and is usually expressed as a percentage. Eqn 4.1 is not an exhaustive list of possible errors; errors can be introduced by a number of additional factors, including but not limited to incomplete uv sampling, deconvolution and flux absorption. As a result, the spectral index calculated and reported in literature should be thought of as a lower limit (Van Weeren et al., 2019).

The integrated spectra of giant radio halos is typically steep, and fall within $-1.4 < \alpha < -1.1$, where $S_\nu \propto \nu^\alpha$. A spectral index with $\alpha \lesssim -1.6$ is considered to be ultra-steep spectrum radio halos (USSRH). Such sources are subject to a cut-off frequency, ν_b, which, according to the turbulent re-acceleration model, scales as

$$\nu_b \propto \left(1 + \frac{\Delta M}{M}\right)^3 \tag{1.5}$$

In a cluster merger event, where M is the mass of the main cluster and ΔM is the mass of the subcluster; indicating that a radio halo will become very steep when observed at ν_b or greater. As such, USSRHs are considerably more detectable when observed at frequencies $<< \nu_b$ in a less energetic merger event (Van Weeren et al., 2019).

Power

The power of a radio halo is typically reported at 1.4 GHz, to aid in the study of scaling relations, and is calculated as,

$$P_{1.4\text{ GHz}} = \frac{4\pi (D_L)^2 S_{1.4\text{ GHz}}}{(1+z)^{\alpha+1}} \tag{1.6}$$

where D_L is the luminosity distance, $S_{1.4\text{ GHz}}$ is the integrated flux density scaled to 1.4 GHz, and $(1+z)^{\alpha+1}$ is the *k-correction*, with typical powers ranging from $10^{23} - 10^{26}$ W Hz^{-1} (Van Weeren et al., 2019, Knowles et al., 2022).

There are less than 100 radio halos currently known. Notable cases of radio halos are that of the double-halo cluster pairs in the pre-merger phase, Abell 1758N - Abell 1758S and Abell 399 - Abell 401.

1.3.2 Mini Radio Halos

Mini radio halos, or simply mini-halos, are smaller ($\lesssim 500$kpc) than giant radio halos, and share few similarities. The synchrotron volume emissivities of mini-halos are higher than that of giant radio halos, with the emission being mostly bound to the X-ray cooling region. Mini-halos are thus difficult to classify without corresponding X-ray data. It is challenging to separate mini-halos from other, similar radio emissions, such as core-halos and lobe-like, centrally located structures. With the addition of bright central radio galaxies and the detection limit of current radio telescopes, the classification of mini-halos can prove to be quite challenging (Van Weeren et al., 2019).

Morphologies

Mini-halos are diffuse radio sources, typically $\sim 100 - 500$ kpc, and centrally located within galaxy clusters. Mini-halos are typically found in relaxed (undisturbed), cool cores of clusters, where their size is analogous to that of the cooling regions of the central cluster. A typical mini-halo can be seen in Figure 1.4.

Origins of Mini-Halos

Mini-halos require in-situ acceleration, as giant radio halos do, due to the short lifetime of their synchrotron-emitting electrons (Van Weeren et al., 2019). Similarly to giant radio halos, the origin of mini-halos can be explained with either the hadronic model, or the turbulent reacceleration model being responsible for the presence of the synchrotron emitting electrons (Van Weeren et al., 2019). However, in the case of the turbulent re-acceleration model, the turbulence causing mini-halos is currently thought to originate via the sloshing of ICM gas with seed electrons, rather than being induced by merger events (Duchesne et al., 2021). This is due to mini-halos being restricted by cold fronts (Mazzotta & Giacintucci, 2008). Unlike giant radio halos, there has been no firm evidence against the hadronic model for the formation of mini-halos.

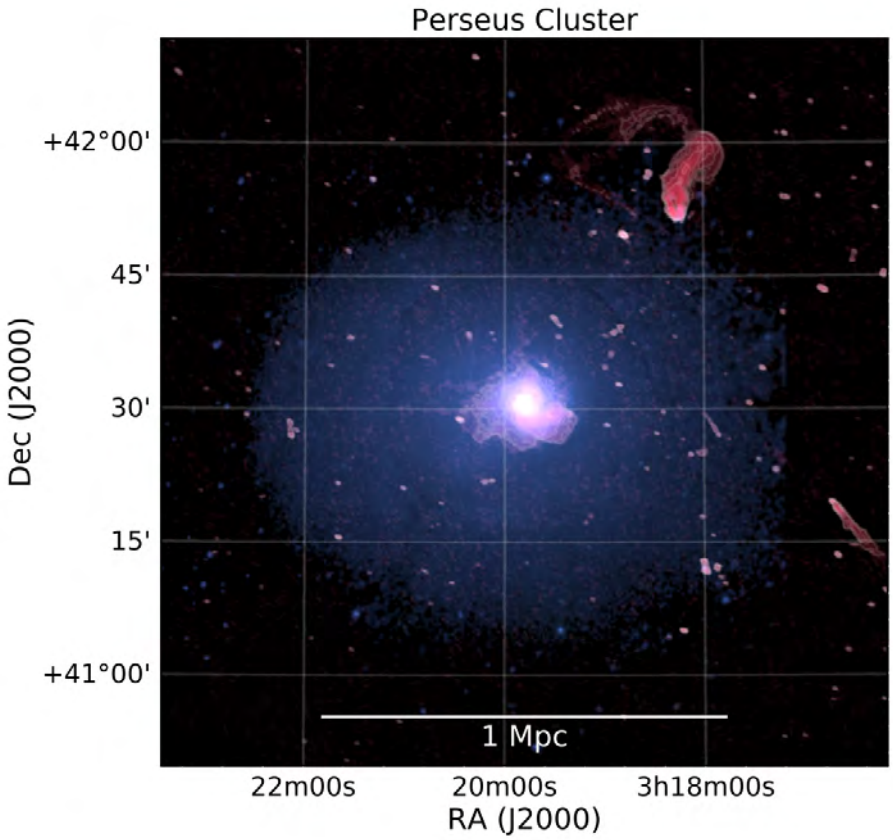

Figure 1.4: The Perseus cluster, hosting a mini-halo. Radio emission (red) is 230–470 MHz VLA data, and X-ray emission (blue) is XMM-Newton data. Image taken from Gendron-Marsolais et al. (2017).

Power

The power of mini-halos is calculated as in Equation 1.6, and has typical values of $10^{23} - 10^{25}$ W Hz^{-1}. Unlike giant radio halos, there has not been a correlation detected between cluster mass and mini-halo power (Van Weeren et al., 2019). Giacintucci et al. (2017) found that in a sample of 58 mass-limited clusters ($M_{500} > 6 \times 10^{14} M_{\odot}$), 12 out of 15 (80%) cool core galaxy clusters hosted mini-halos. This indicates that mini-halos are common in such systems.

1.3.3 Unification of Mini-Halos and Giant Radio Halos

Recent studies have indicated that it is possible that mini-halos evolve into giant radio halos, and vice-versa. This could be caused by a transition between either turbulent re-acceleration due to core-sloshing or hadronic mini-halos and merger-induced turbulent re-acceleration for giant radio halos (Van Weeren et al., 2019). Bonafede et al. (2014) found a giant radio halo with a strong cool core. Such an instance could indicate that a mini-halo would be present when a merger has not yet caused the disruption of the cool cluster core. Once the core is disturbed, the mini-halo turns off, and the formation of a giant radio halo begins. This is just one example of a peculiar case that indicates the possibility of transitions between giant radio halos and mini-halos, depending on the merger state of a galaxy cluster.

1.3.4 Radio Relics

Cluster radio shocks, or radio relics, are diffuse sources that are found in cluster outskirts, and have been identified in clusters with a wide range of masses. Radio relics are strongly polarised at frequencies $\gtrsim$ 1GHz compared to other types of diffuse emission, due the compression of the magnetic fields at shock fronts (Van Weeren et al., 2019).

Morphology

Radio relics have an elongated morphology, which is believed to trace shock waves in cluster outskits. They range in size from $0.5 - 2$Mpc, while larger radio relics show asymmetric bright-

ness profiles, with gradually fading emission on the side closest to the galaxy cluster and rapidly fading emission on the other side. Larger radio relics also show the strongest polarisation.

Deep studies of several radio relics have found a ubiquitous filamentary-like structure that potentially traces the magnetic field fluctuations (Van Weeren et al., 2019) .

An interesting subclass of radio relics is the *double shocks*, where two large elongated radio relics are found opposite one another with the cluster core being at the centre. This pair of radio relics are generated at the same time during a core passage. This subclass is important as it can constrain the cluster merger scenario fairly well (Van Weeren et al., 2019). Several of these systems are known. Roettiger et al. (1999) found that these sources could be caused by particles being accelerated at shocks caused by a binary merger.

Origins of Radio Relics

Fermi I acceleration, also known as Diffusive Shock Acceleration, occurs at a shock front (Van Weeren et al., 2019). Energy injected into the ICM from the shock accelerates particles diffusively at the shock front during Fermi I acceleration. Electrons at the edge of the shock front are scattered forwards and backwards, allowing the particles to gain kinetic energy, and thus, be accelerated (Hoeft & Brüggen, 2007). The Fermi I mechanism is not an efficient mechanism, however, as it can not energise the particles quickly enough, and the increase in energy is limited by how energetic the shock is.

In an idealised merger, shocks move along the merger plane, followed by dark matter passage, and then by merger shocks. The amount of kinetic energy that is dissipated in merger shocks increases with distance from the cluster centre. This, along with the geometric orientation of radio relics, results in observed radio relics being located in cluster outskirts (Vazza et al. (2012); Van Weeren et al. (2019)). Cluster outskirts are a lower-density environment and as such, it is believed that electrons in the outskirts of clusters are energised from the ICM via diffusive shock acceleration (Fermi I mechanism). The electrons are accelerated to relativistic speeds by Diffusive Shock Acceleration, and result in synchrotron emission in the form of radio relics, and

as a result, radio relics are believed to form from shock-accelerated electrons (Botteon et al., 2018; Duchesne et al., 2021).

Radio Spectra

The integrated spectra of radio relics are found to be $-1.0 \leq \alpha \leq -1.5$, and show power-law shapes. Radio relics show a clear spectral gradient across the width of the source, with the steeper spectral index facing the cluster centre, and the flatter spectral index facing away from the cluster centre. This is believed to be caused by the synthron losses in the region closest to the cluster centre, resulting in a steeper spectrum (Van Weeren et al., 2019).

1.3.5 Radio Bridges

Diffuse radio emission extending regions even greater than that of radio halos have been detected by the LOFAR telescope. This extended diffuse emission appears to be bridging between two galaxy clusters in a pre-merger phase, and contains relativistic electrons and magnetic fields generated on unprecedented scales. These regions are likely filled with compressed gas and have been aptly named *radio bridges* (Brunetti & Vazza, 2020). To date, only two radio bridges at such a large scale, situated between galaxy sub-clusters, have been confirmed, namely Abell 399-401 (Govoni et al., 2019) and Abell 1758 (Botteon et al., 2020), which will be discussed further in Section 1.4.

Radio bridges have become an object of new interest, as recent studies (Govoni et al., 2019; Botteon et al., 2018) have indicated that a radio bridge represents an essential stage in cluster mergers, whereby the remains of the bridging cosmic filament is compressed and pre-processed by gas dynamics. This phenomenon should occur in all major merger events before the merger of the galaxy clusters (Brunetti & Vazza, 2020). Radio bridges also indicate the existence of non-thermal components at considerable distances from the cluster centres (Botteon et al., 2020).

Origin of Radio Bridges

The origin of radio bridges may be related to the turbulence generated by the ICM during the pre-merger phase of galaxy clusters. The turbulence enhances the radio and X-ray emission between galaxy clusters (Botteon et al., 2020), creating the diffuse emission we know as radio bridges. The areas between clusters are the most dilute part of the ICM that we are able to study with our current tools (Vazza et al., 2019).

In the case of radio bridges, it is believed that the Fermi II mechanism is the most likely reacceleration mechanism, reaccelerating pre-existing and volume-filling thermal electrons to radio-bright energies (> GeV Brunetti & Vazza, 2020). The most promising way to learn more about the physics of reacceleration mechanisms is by studying the spectral index of the radio emission observed. The spectral index, α (see Eqn. 1.3), can discriminate the two models. A spectral index of $\alpha > -1.4$ generally indicates the Fermi I mechanism, while the Fermi II mechanism can produce much steeper spectral indices, $\alpha < -1.4$. Thus, by studying the spectral index of a source, we can constrain the particle acceleration mechanism.

1.4 A Few Special Cases

1.4.1 The Abell 399 - 401 pair

The Abell 399 - Abell 401 (hereafter, A399-401) is a galaxy cluster pair at redshift $z = 0.072$, with a gas temperature of $kT \approx 7$ keV and $kT \approx 8$ keV respectively. They are separated by a 3 Mpc prjected distance. Early X-ray observations detected a slight temperature increase in the region between them, indicating a dynamical interaction (Fujita et al., 1996; Fabian et al., 1997; Markevitch et al., 1998) and more recent observations suggested that the two clusters are in an early merger phase (Fujita et al., 2008; Akamatsu et al., 2017). Bonjean et al. (2018) and Hincks et al. (2022) confirmed the presence of connecting bridge between the two clusters, deriving a 4.3×10^{-4} cm^{-3} gas density from Sunyaev-Zeldovich observations.

Radio observations at 1.4 GHz detected radio halos in both clusters (Murgia et al., 2010).

The double radio halo was initially unexpected, as radio halos were thought to be uncommon in early merger phases, when the bulk of the kinetic energy due to collisions has not yet been dissipated.

Recent observations at 140 MHz revealed a filament of diffuse synchrotron emission between the clusters Govoni et al. (2019). This was the first instance of extended radio emission on a Mpc scale, bridging between clusters. The filament has a projected length of 3 Mpc, and can be seen clearly bridging between A399 and A401 in Figure 1.5.

The bridge has a peak brightness of 3.7 mJy beam^{-1} with an average surface brightness $\tilde{I}_{140} = 2.75 \pm 0.08$ mJy beam^{-1} and an integrated flux density of 822 ± 24 mJy (Govoni et al., 2019). The existence of radio emission on such large scales poses a question related to their acceleration mechanism. Like radio halos in galaxy clusters, the lifetime of particles due to synchrotron losses is $\sim$ 200 Myr over which electrons could only travel as far as $\sim$ 0.1 Mpc, i.e. they would have radiated their energy away over the bridge extension. Govoni et al. (2019) explores the possibility that shock waves generated in the bridge region due to the dynamical interactions can re-accelerate a pool of thermal and fossil electrons (Wittor et al., 2019). They notice that the population of fossil relativistic electrons (with a Lorentz factor of the order of 10^3) is necessary to generate synchrotron emission as the acceleration efficiency due to shocks is too small to directly accelerate thermal electrons to relativistic energies.

Brunetti & Vazza (2020) proposes a different scenario, where particles are accelerated by the scattering with magnetic field lines that diffuse in super-Alfvenic turbulence, which also amplifies magnetic fields. In this case, steep-spectrum synchrotron emission can fill the entire intracluster bridge region, with a spectral index greater than $\alpha < -1.3$. The expected synchrotron spectral index would, instead, be $-1.2 < \alpha < -1$ in the case that particles are accelerated via shocks, therefore spectral index measurements can disentangle between the two acceleration scenarios. Spectral index measurements of the bridge emission are therefore necessary to understand the particle acceleration mechanism in action.

Recent observations at 350 MHz did not detect the bridge, therefore placing an upper limit

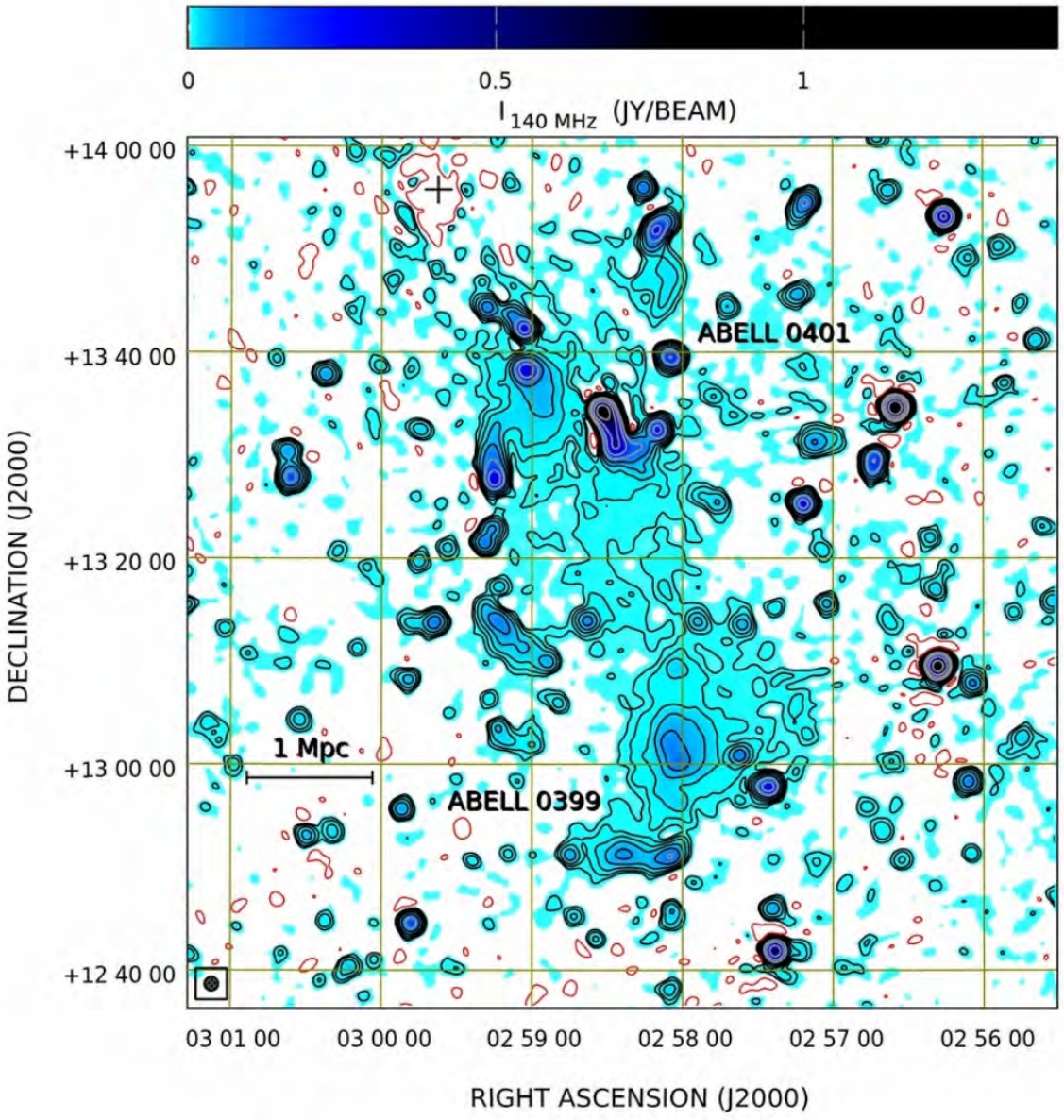

Figure 1.5: Image of the A 399 – A 401 system at 140 MHz, with a resolution of 80" and sensitivity of 1 mJy beam^{-1}. The radio bridge is clearly visibile in between clusters (Govoni et al., 2019).

on the steepness of the spectral index $\alpha < -2.2$ at 95% confidence level (Nunhokee et al., 2023; Pignataro et al., 2023). Such upper limits disfavour the shock acceleration scenario whereas they are still consistent with the expectations of the turbulent reacceleration model.

The bridge was found to be unpolarized at 140 MHz suggesting that if the radio emission is generated by shocks, a depolarizing mechanism must be in place (Balboni et al., 2023). If depolarization is due to a Faraday screen in front of the shocks, then the magnetic field ought to be larger than 0.46 nG, consistent with what is expected in cosmological simulations (Vazza et al., 2019).

1.4.2 Abell 1758

The galaxy cluster Abell 1758 (A1758) has a redshift of $z = 0.279$, and consists of two components, a Northern and Southern subcluster, (hereafter, A1758N and A1758S, respectively) separated by a distance of ~ 2 Mpc (Rizza et al., 1998). David & Kempner (2004) estimated a virial radius of 2.6 Mpc and 2.2 Mpc for A1758N and A1758S respectively. X-ray observations indicated that the subclusters are gravitationally bound and found no noticeable interaction between the two subclusters, although they are undergoing their own mergers (David & Kempner, 2004).

A1758N hosts extended diffuse emission in the form of a extended radio halo reaching ~ 2.2 Mpc at the largest linear size, observed at 140 MHz, with an integrated spectral index $\alpha = -1.2 \pm 0.1$ (Botteon et al., 2018). A1758S also hosts a radio halo with a $\alpha = -1.1 \pm 0.1$ spectral index. The radio emission that sits on the outskirts of A1758S was classified as a potential radio relic, with a spectral index of $\alpha = -1.3 \pm 0.1$ (Botteon et al., 2018). Follow up observations revealed the presence of a radio bridge connecting both subclusters (Figure 1.6; Botteon et al., 2020). The bridge is mostly visible at 144 MHz, partly at 53 MHz and invisible at 383 MHz and 1.5 GHz. In the top left image of Figure 1.6, the white box surrounding a filament-like structure indicates the area over which the flux densities were integrated at 53 MHz and 144 MHz image, to derive a spectral index $\alpha = -1.65 \pm 0.27$ (Botteon et al., 2020). However, if a 3σ limit

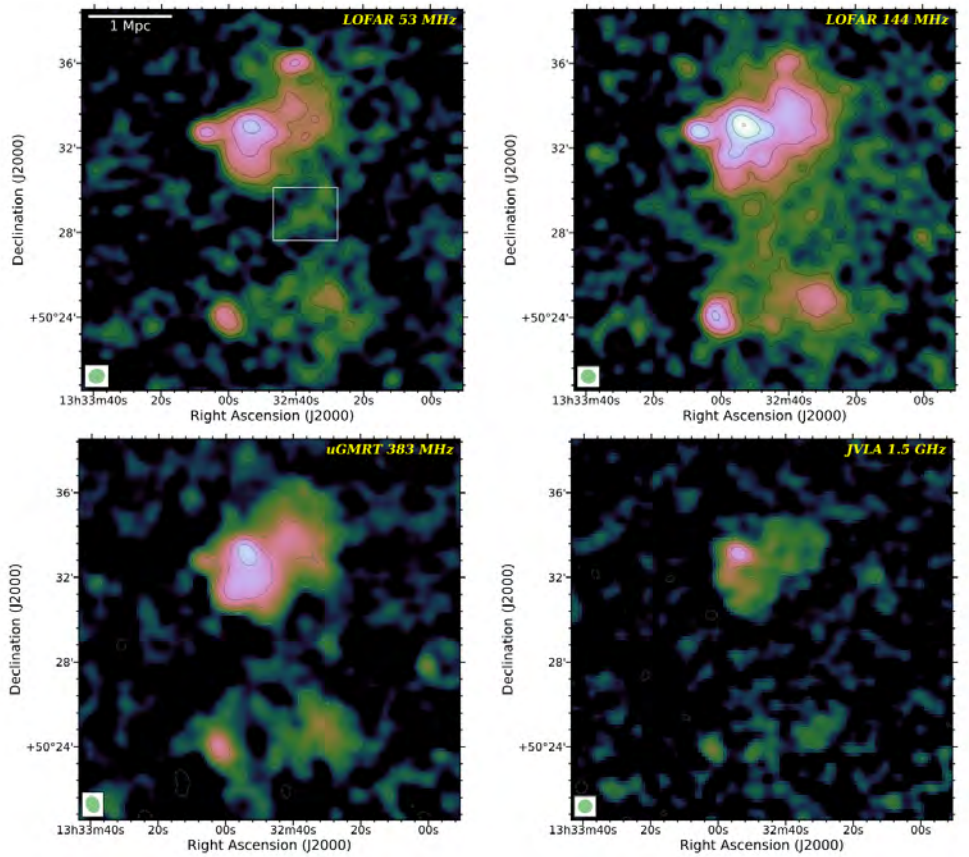

Figure 1.6: Images of the radio bridge in A1758 at 53 MHz (top left panel), 144 MHz (tp right panel), 383 MHz (bttom left panel) and 1.5 GHz (bottom right panel), respectively (Botteon et al., 2020).

is assumed for the 53 MHz emission, the spectral index over the entire radio bridge would be constrained t be $\alpha > -1.87$. Given the non detection at 383 MHz and 1.5 GHz the spectral index would be in the range $-1.87 < \alpha < -0.4$ (Botteon et al., 2020).

As discussed for the A399–A401, turbulent motions from complex dynamics between pre-merging clusters may accelerate electrons and, consequently, generate the radio emission observed in bridges. In such a model, the emission from radio bridges at lower frequencies would need to be volume-filling. The detection of the radio bridge in A1758 at 144 MHz is consistent with this model, in particular the strong correlation between the radio and X-ray emission

suggests that the thermal and non-thermal emission of the radio bridge originates from similar volumes (Botteon et al., 2020). The spectral index measurements, however, do not rule out completely a shock or a turbulent scenario.

1.4.3 Abell 141

Abell 141 is a galaxy cluster at a redshift of $z = 0.23$ (Struble & Rood, 1999), with an SZ-derrived mass of $5.67^{0.36}_{-0.40} \times 10^{14}$ $M_\odot$ (Ade et al., 2016). A 141 has been previously observed and studied in optical, X-ray and radio regimes. Optical and X-ray maps reveal a bi-modal structure (Caglar, 2018), which can be seen in Fig. 1.7. X-ray observations of A 141 indicate two subclusters, one located in the North and the other in the South of the cluster (A 141N and A 141S, respectively), separated by a projected distance of 2.7 Mpc (Caglar, 2018). A 141N is considered the primary subcluster, as it is brighter, denser and more massive than its Southern counterpart, and hosts a centrally-located diffuse radio halo, detected at 168 MHz (Duchesne et al., 2021).

X-ray observations indicate that A 141N and A 141S are not only in a pre-merger state, but that they are in a later stage of a pre-merger, as the subclusters have not completed a core-crossing. The cores of A 141 subclusters will likely meet within $0.23 - 0.42$ Gyr. Additionally, there is an X-ray hotspot between the subclusters which could imply the presence of a shock, from which a Mach number of $\mathcal{M}_X = 1.69^{+0.41}_{-0.37}$ can be derived (Caglar, 2018).

A 141 was first studied in the radio regime by Venturi et al. (2008), who reported a non-detection of a radio halo at 610 MHz. Duchesne et al. (2021) observed a giant radio halo at 168 MHz, and, using the upper limit from Venturi et al. (2008), constrained the spectral index to be $\alpha < -2.1$, potentially very steep. More recent observations of A 141 in the $88 - 943$ MHz range found clear evidence of central diffuse emission as well as an extended emission in the form of a peripheral structure, the origin of which is uncertain, but resulted in a slightly elongated morphology (Duchesne et al., 2021). They found that the radio emission detected was volume filling between the X-ray subclusters, and measured a mean linear extent of 850 kpc for

the diffuse radio emission. A simple power law was found to describe well the diffuse radio emission between 88 and 943 MHz, with a spectral index $\alpha = -1.06 \pm 0.09$. This value is flatter than previously believed, as a more accurate estimate of the spectral index was derived at low frequencies and with a better subtraction of the discrete source contribution.

Duchesne et al. (2021) performed a radio-X-ray point-to-point correlation analysis, but found no significant correlation between the two. This is atypical for a radio halo hosting galaxy cluster; it may indicate an assortment of emission components, though a lack of correlation has been found to be caused by halos occurring during specific stages of complex mergers (Shimwell et al., 2014).

Duchesne et al. (2021) ultimately classified the emission in A 141 as a radio halo, due to its morphology and spectral index. However, they do mention that while the detected radio emission predominantly coincides with A 141N, it seems to extend towards A 141S, which may suggest a radio bridge. They do note, though, that they do not have the resolution to confirm distinct bridge emissions.

X-ray emission has widely been observed in shocks corresponding to radio relics (Van Weeren et al., 2019). Given that Caglar (2018) identified a spike in the central region temperature, Duchesne et al. (2021) estimated the Mach number of the possible shock:

$$\mathcal{M}_R = \sqrt{\frac{2\alpha_{\text{inj}} - 3}{2\alpha_{\text{inj}} + 1}}, \tag{1.7}$$

where α_{inj} is the synchrotron injection spectrum index, and $\alpha = \alpha_{\text{inj}} - 0.5$. They found $\mathcal{M}_R = 5.9 \pm 0.9$, which is inconsistent with the Mach number derived by X-ray observations (Caglar, 2018). The discrepancy could indicate that seed electrons are accelerated by DSA, as in the instance of radio relics. In this case, $\alpha = \alpha_{\text{inj}}$ and $\mathcal{M}_R = 2.1 \pm 0.2$, in better agreement with $\mathcal{M}_X$. However, Duchesne et al. (2021) could not confirm nor disprove a radio relic with their data.

A power-mass spectrum plots the power of a radio halo (scaled to 1.4 GHz and 0.15 GHz) against the M_{500} mass of the galaxy cluster which hosts the halo, on a set of log-log axes. This

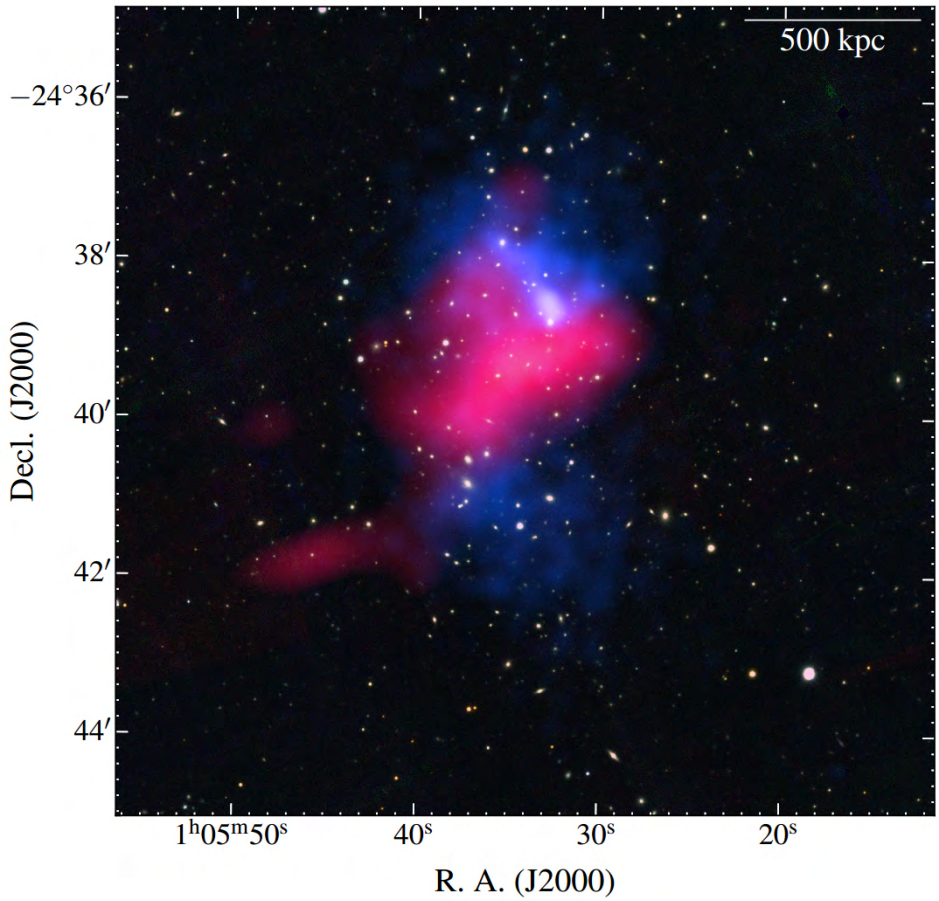

Figure 1.7: A composite image of A 141 (Duchesne et al., 2021). The background is optical data taken from the Pan-STARRS survey, together with Chandra data (blue) and ASKAP data (red).

plot can be used to visualise and compare the power-mass relationship of a radio halo to that of other radio halos. Duchesne et al. (2021) plot A 141 on a power-mass spectrum scaled to 1.4 GHz and 0.15 GHz, along with a contemporary sample of 84 radio halos, and find that when considering it as a single cluster system (i.e. only taking the mass of A 141N, $M_{500} = (3.79 \pm 0.3) \times 10^{14} \mathrm{M}_{\odot}$, A 141 fits within literature values of a radio halo.

1.4.4 Similarities between galaxy clusters hosting radio bridges

All three systems are massive ($\mathrm{M}_{500} \gtrsim 5 \times 10^{14}\ \mathrm{M}_{\odot}$) and consist of a pair of subclusters in pre-merger, where each subcluster is undergoing its own, independent mergers. Additionally, each

system shows an enhancement of the X-ray emission and gas temperature in the bridging region between the subclusters. These similarities are what makes A 141 a good candidate for a radio bridge, or at last, large-scale emission extending beyond the subclusters.

However, both subclusters in the A399-A401 pair and the A1758 pair host a radio halo, while only the Northern subcluster of the A 141 pair hosts a radio halo.

1.5 The MeerKAT radio telescope

The MeerKAT telescope is a radio telescope array located in the Karoo in the Northern Cape province of South Africa (Jonas & MeerKAT Team, 2016), and is a precursor to the Square Kilometer Array (SKA). In this subsection, we will discuss why the MeerKAT telescope is a particularly well suited candidate to study galaxy clusters and, by extension, radio bridges.

The Northern Cape province of South Africa was chosen for its particularly sparse population, indicating that there would be little human-made radio frequency interference (RFI). RFI is a continuous problem in radio astronomy, where man-made radio signals, such as Bluetooth, Wifi, and radio broadcasting, to name a few, interfere with the faint radio emission received from celestial sources. Due to its nature, RFI tends to follow the population of people, with population-dense areas having the most amount of RFI. In addition to its sparse population, the location of the MeerKAT telescope also has neighbouring mountains to the South, providing extra protection from the RFI that would emanate from nearby areas of high population.

The MeerKAT array consists of 64 offset Gregorian radio antennas, a schematic of which can be seen in Figure 1.8, each with a diameter of 13.5 m (Jonas & MeerKAT Team, 2016). Each antenna hosts two receivers, which allow for two separate observing bands, namely the *UHF-band*, and the *L-band* (Table 1.1). Both of these bandwidths have 4096 channels, where each channel has a width of $\sim$ 209 kHz. The numerous channels allow for the precise removal of RFI.

In radio interferometry (See Chapter 2), a *baseline* refers to the separation between two

Frequency Band	UHF band	L-band
Frequency Range (MHz)	580 – 1015	900 – 1670
Bandwidth (MHz)	544	856

Table 1.1: MeerKAT receiver bands (Jonas & MeerKAT Team, 2016).

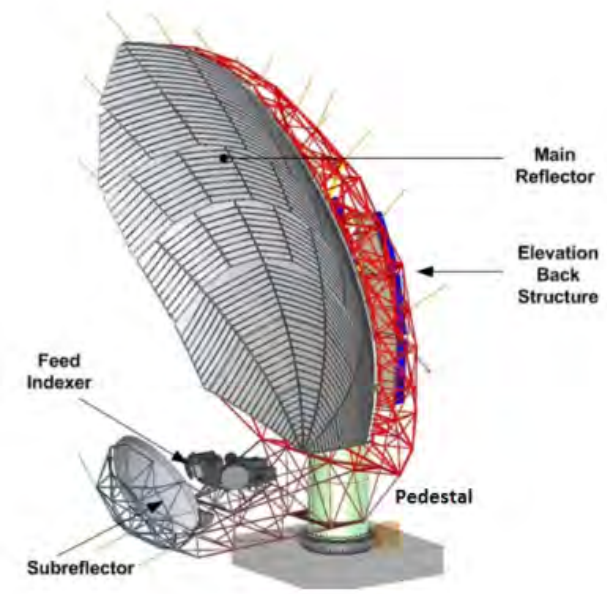

Figure 1.8: A diagram of the Gregorian off-set conofiguration used fr MeerKAT (Jonas & MeerKAT Team, 2016).

antennas. Short baselines are used to study large-scale, diffuse emission, while longer baseline are used to resolve compact sources with high resolution. The arrangement of the MeerKAT antennas is such that 70% of the antennas are within a 1 km radius, with baselines ranging between 29 m, the shortest baseline, and 1 km to create a compact core. The remaining 30% of antennas are placed further out to a maximum distance of 7.6 km (Booth et al., 2009).

The configuration of the MeerKAT telescope is what makes it an efficient tool to study galaxy clusters. Long baseline allow for high-resolution imaging of galaxy cluster structures, and the dense core of the antennas allows for sensitivity towards diffuse and low surface brightness emission, the type of emission associated with the ICM and found in galaxy clusters.

In this project, in particular, the compact antenna core will allow for the study of diffuse emission of the A 141 cluster, while the high resolution achieved by the long baselines will allow for accurate source subtraction, which is necessary to study the diffuse emission fully.

1.6 Thesis Motivation

A 141 hosts large-scale radio emissions, potentially in the form of either a giant radio halo and/or a radio bridge. In this thesis, we will study the radio emission in A 141 using MeerKAT observations with the aim of improving on previous observations both in terms of sensitivity and angular resolution. This will allow for a more precise understanding of the diffuse radio emission associated with this galaxy cluster.

In particular, previous studies found a radio halo hosted by the Northern subcluster, as well as hints at diffuse radio emission extending towards the Southern subcluster. We aim to characterize the morphology of the radio emission in between the two subclusters. This will allow assessment of the presence of a radio bridge, which is at present unclear from current observations.

Finally, we aim to characterize the spectral properties of the diffuse emission in order to shed light on the mechanism behind particle re-acceleration. Recent studies by Duchesne et al. (2021) find a somewhat flat spectral index, which contradicts predictions made by current re-acceleration theory simulations (Brunetti & Vazza, 2020). In this thesis, we aim to improve the spectral index measurement and to compare it with the value previously reported. This will aid in the understanding of particle acceleration mechanisms. Additionally, these observations at 1.28 GHz will provide another frequency point to test the consistency of the power-law spectrum previously reported.

CHAPTER 2

Radio Technologies and Techniques

Angular resolution is the minimum distance θ at which two sources can still be seen as separate, and is defined using Rayleigh's criterion,

$$\theta \approx 1.22 \frac{\lambda}{D}, \tag{2.1}$$

where

D is the telescope diameter and λ is the observing wavelength. The smaller the value of θ, the better the angular resolution. Thus, we seek to minimise θ for maximum angular resolution. Assuming a circular aperture, the aperture (A) of the dish relates to the diameter (D) as,

$$A \propto D^2. \tag{2.2}$$

As such, a larger dish will result in a higher angular resolution.

2.1 Single Dish Radio Astronomy

Several radio astronomical observations use a single dish antenna, that generally has a parabolic shape. The parabolic dish shape allows for electromagnetic waves emitted from celestial bodies to be collected and focused toward the centre, where the receiver sits (Geyer et al., 2016).

An example of a single-dish radio telescope is the Green Bank Telescope (GBT) located in the United States of America. The GBT, completed in 1999, hosts a fully steerable single antenna with a diameter of 100 m (Lockman, 1998). A large dish is desirable to achieve high angular resolution, and while a 100 m radio telescope is not a simple feat, the want for an even larger dish arose. Thus, the Five-hundred-meter Aperture Spherical radio Telescope (FAST) was completed in 2016. Due to the limitations imposed by the sheer size of its dish, the telescope was built in a natural concave, to support the 500 m diameter. While this places its own limitation on the telescope, such as fixing the antenna in place, the receiver is mobile, and thus allows for more flexibility in the pointing direction (Nan et al., 2011). This was an effective mitigation of the physical limitations of the fixed telescope, and succeeded in increasing the angular resolution when compared to the predecessors of FAST.

The construction of increasingly larger single-dish telescopes soon becomes unfeasible, from both a technical and a cost perspective. However, single dish telescopes are still in use, and are often used in combination with interferometric arrays, as is the case in Vacca et al. (2022) and Loi et al. (2017), where a single-dish radio telescope is used in tandem with a radio interferometer to provide information on the largest angular scales not sample by interferometric observations. In the next chapter, we will describe interferometric arrays, which can achieve the highest angular resolution in radio astronomy.

2.2 Fourier Transform

Before summarizing radio interferometry, it is useful to recap a few concepts about Fourier transforms that lie at the essential core of it.

Fourier Theory states that any signal can be decomposed into a number of sinusoids, each with a different frequency, which will sum up to the original signal. That is, every signal can be represented by a sum of cosines and sines, each with a different co-efficient, known as a Fourier *mode*. A Fourier transform is then a reversible, linear mathematical operation that decomposes the signal into its Fourier modes (Hoffman, 1997). The Fourier transform of a function $f(x)$ as defined as (e.g., Thompson et al., 2017a):

$$F(s) = \int_{-\infty}^{\infty} f(x)\, e^{-j2\pi sx}\, dx, \tag{2.3}$$

and the inverse of $F(s)$ is given as

$$f(x) = \int_{-\infty}^{\infty} F(s)\, e^{j2\pi sx}\, ds, \tag{2.4}$$

such that the two can be written symbolically as

$$f(x) \longleftrightarrow F(s). \tag{2.5}$$

If x has units of u, s will have units of inverse of u. That is if x has units of the time domain, such as $seconds$, s will have units of $second^{-1}$, i.e. Hertz (Thompson et al., 2017a). This gives a Fourier transformation pair used to transform between the time and frequency domains.

Fourier transforms have a few important properties. One property of particular interest to us is the convolution theorem. The convolution theorem states that the Fourier transform of the convolution of two functions, say $f(x)$ and $h(x)$, is simply the product of their individual Fourier transforms (e.g. Hoffman, 1997),

$$\mathscr{F}\{f(x) \otimes h(x)\} = F(s)H(s). \tag{2.6}$$

Simply put, the point-wise product of two functions in one domain is equal to the convolution of the two functions in the other domain.

In the context of interferometric radio astronomy, to compute a continuous signal, it is necessary to take the Fourier transform of the signal. However, computational devices, such as computers, can only process discrete data. For this reason, it is necessary first to get a discrete set of samples from the signal. This can be done by using the *Discrete Fourier Transform* (DFT).

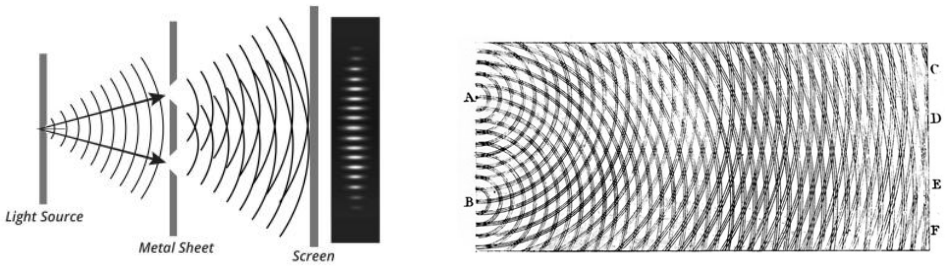

Figure 2.1: Left: Schematic of the double slit experiment (Image taken from https://www.discovery.com/science/Double-Slit-Experiment) conducted by Thomas Young in 1803. Right: Thomas Young's sketch of the interference patterns of light waves.

The DFT, F, of a function f is defined as:

$$F_r = \sum_{k=0}^{N_0-1} f_k \, e^{-ir(\frac{2\pi}{N_0})rk}, \tag{2.7}$$

where N_0 is the number of samples in one period (T_0) of the signal.

2.3 Radio interferometry

Interferometry dates back to the famous double-slit experiment conducted by Thomas Young in 1803. In this experiment, a light source was shone onto a metal sheet with two slits in it, as shown in Figure 2.1. The light waves interacted with one another, and their interference pattern was projected onto a screen, showing a fringe pattern (Figure 2.1; Young, 1807). The fringe pattern is sensitive to the distance between the slits, the wavelength of the incident light as well as the phase delay, introduced by the difference in path length travelled by the light from the slit to the screen (Geyer et al., 2016).

Interferometry is commonly used in radio astronomy to combine signals from different telescopes. The simplest interferometric array is the two-element interferometer (Figure 2.2), where the signals received from two antennas are combined to create an interference pattern, known as the *antenna response*, which is studied to extract information about the celestial source. The celestial signal collected by antenna 1 is delayed with respect to antenna 2 by a time delay τ_g that

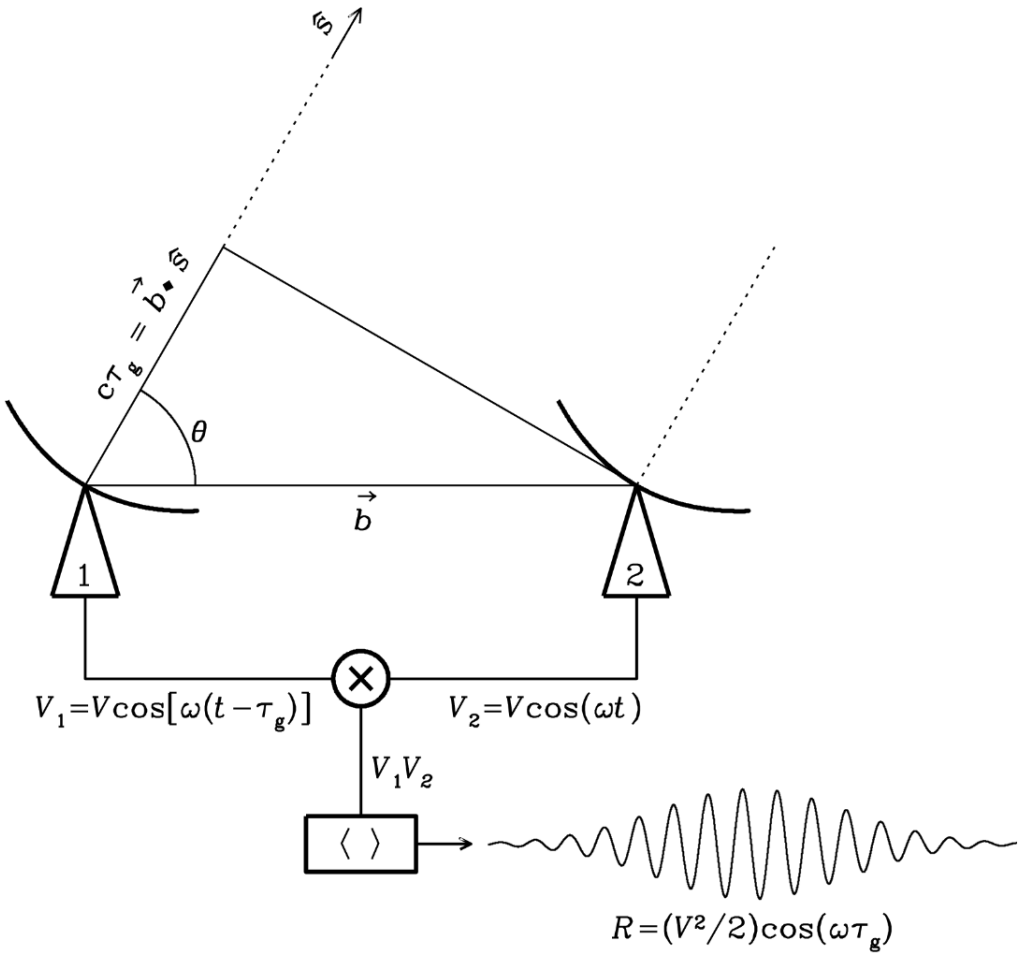

Figure 2.2: The two-element interferometer. The celestial signal reaches antenna 1 later than antenna 2 and the corresponding delay is proportional to the baseline separation b (Condon & Ransom, 2016).

is proportional to the distance between them,

$$\tau_g = \frac{\vec{b} \cdot \hat{s}}{c}, \tag{2.8}$$

where $\hat{s}$ is the direction of the incoming celestial signal and b baseline. If we describe the voltage induced by the celestial signal at the antenna 2 as a generic sinusoidal function $V_2 = V \cos \omega t$, then the signal at the antenna 1 becomes $V_1 = V \cos \omega(t - \tau_g)$. The correlator then combines them to create a response $R \propto V^2 \cos \omega \tau_g$ (Condon & Ransom, 2016). If two polarisations are measured by each antenna, the correlator produces four *cross-correlation* products, referred to as *visibilities*. Visibilities V are related to the sky brightness distribution by the van Cittert-Zenike theorem, which states that the spatial visibility is the Fourier transform of the intensity distribution:

$$V(u, v, w) = \int_\Omega I(l, m)\, e^{-2i\pi(ul+vm+w(n-1))}\, \frac{dldm}{n}, \tag{2.9}$$

where the relationship between the visibility coordinates (u, v, w) and image plane coordinates (l, m) are shown in Figure 2.3. For an interferometer with N antennas, there will be $\frac{N(N-1)}{2}$ independent, and likely unique, baselines. Even in the case of large N values, the number of different (u, v) points measured will always be limited and, therefore, the sampling of the sky brightness distribution is incomplete. One commonly adopted way to improve the (u, v) coverage is through Earth rotation synthesis: as the earth rotates, the baseline length and orientation change and its corresponding (u, v) coordinate changes too, creating what is called a *(u,v) track*; an example of the (*u,v*) tracks for our MeerKAT data set can be seen in Figure 2.4.

Each baseline will have a unique (*u,v*) track: when all $\frac{N(N-1)}{2}$ baselines are combined, the result is the *(u,v) sampling* function, $S(u, v)$

Equation 2.9 can be formally inverted to obtain the sky brightness distribution I:

$$I_\nu(l, m) = \int_{\Omega'} V(u, v)\, e^{-2i\pi(ul+vm)}\, du\, dv = \tag{2.10}$$

$$= \mathscr{F}^{-1}[V(u, v)], \tag{2.11}$$

where we assumed the so-called flat sky approximation, i.e. $n = 1$. As the visibilities are

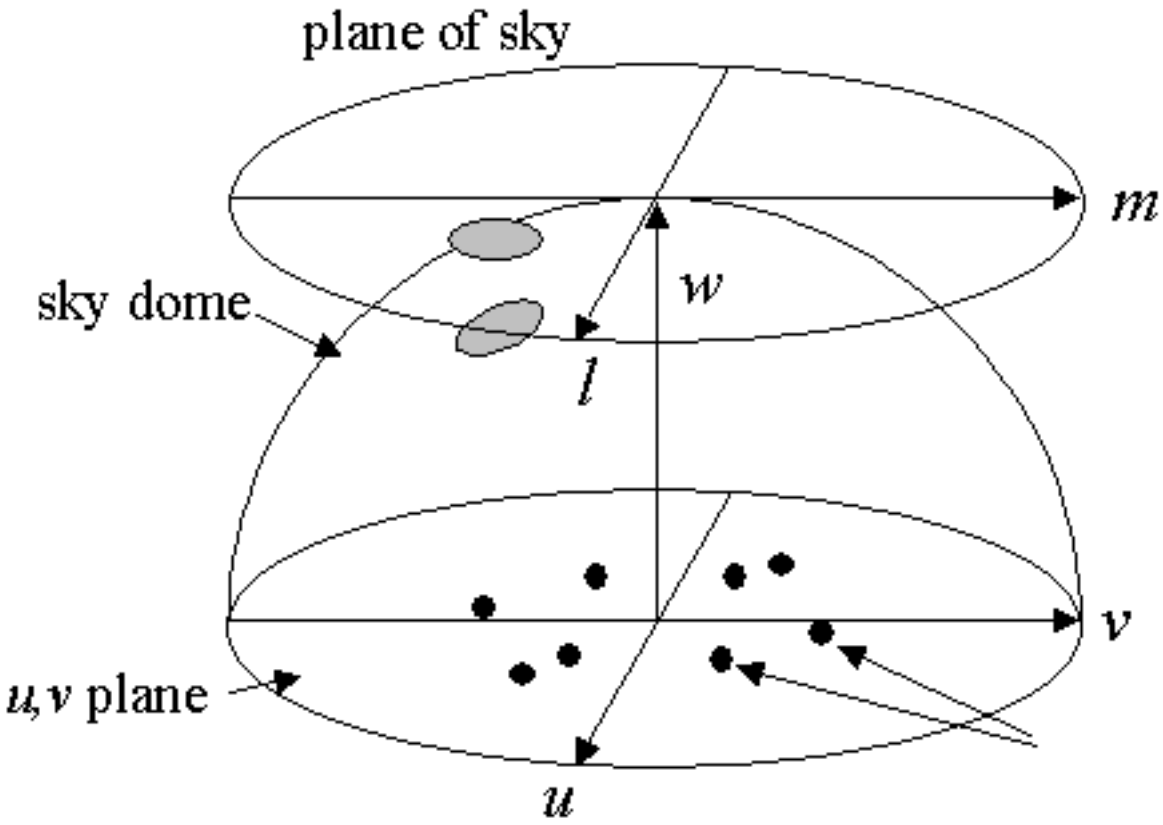

Figure 2.3: The relationship between visibility and image plane coordinates (https://web.njit.edu/~gary/728/Lecture6.html).

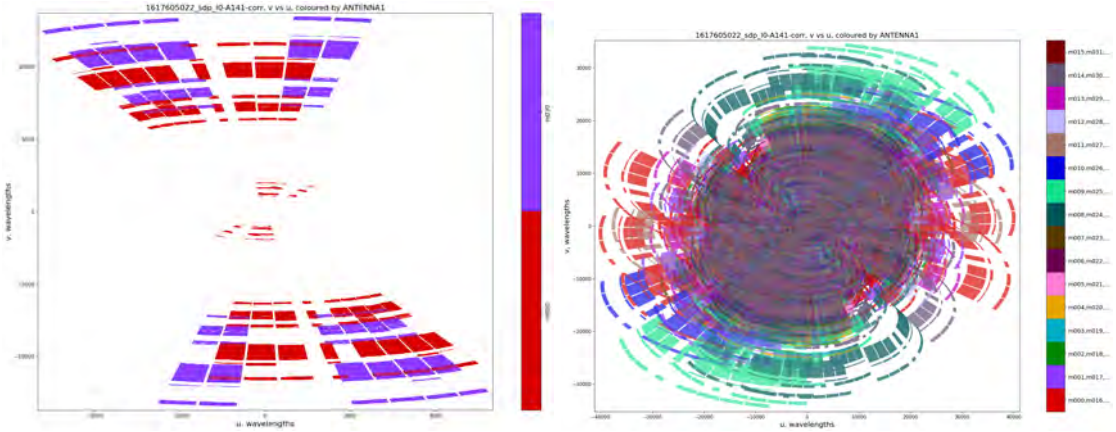

Figure 2.4: (u,v) tracks of two baselines, and complete u,v-coverage when all the baselines are included for our MeerKAT data set.

measured at a certain number of (u, v) points, the actual inversion should be written as:

$$I_\nu^D(l, m) = \mathscr{F}^{-1}[V(u, v)S(u, v)], \tag{2.12}$$

where I_ν^D is the *dirty image*, named as such as it is affected by the sampling function. If we recall the convolution theorem (Section 2.2), equation 2.12 can be written as:

$$\mathscr{F}[V(u, v)S(u, v)] = \mathscr{F}[V(u, v)] \otimes \mathscr{F}[S(u, v)]. \tag{2.13}$$

Bearing in mind that the Fourier transform of the visibility function is the true sky brightness

$$\mathscr{F}[V(u, v)S(u, v)] = I_\nu(l, m) \otimes \mathscr{F}[S(u, v)], \tag{2.14}$$

where the convolution of the sampling function is called the *point spread function* (PSF; figure 2.5). The PSF has, generally, sidelobes due to the incomplete (u, v) sampling, therefore, a better reconstruction of the sky brightness distribution requires the deconvolution of the dirty image from the point spread function.

The deconvolution is usually performed iteratively through the the CLEAN algorithm (Högbom, 1974) as follows:

1. identify the brightest pixel and its location in the dirty image. This corresponds to the strongest source in the dirty image;

2. create a *model image*. The model image is initially empty and is subsequently populated at the pixel location where sources are found in the dirty image;

3. subtract the scaled PSF from the dirty image at the point of the brightest pixel. The scaled PSF corresponds to the PSF multiplied by the brightest pixel times a gain loop factor, γ, which expresses the fraction of flux to be subtracted. Typical loop gain factors are 0.1 or 0.2. The subtraction also reduces the contribution of the PSF from the source in the image, ideally revealing fainter sources that were hidden underneath the sidelobes of bright sources;

4. a *residual image* is formed after the scaled PSF is subtracted from the dirty image.

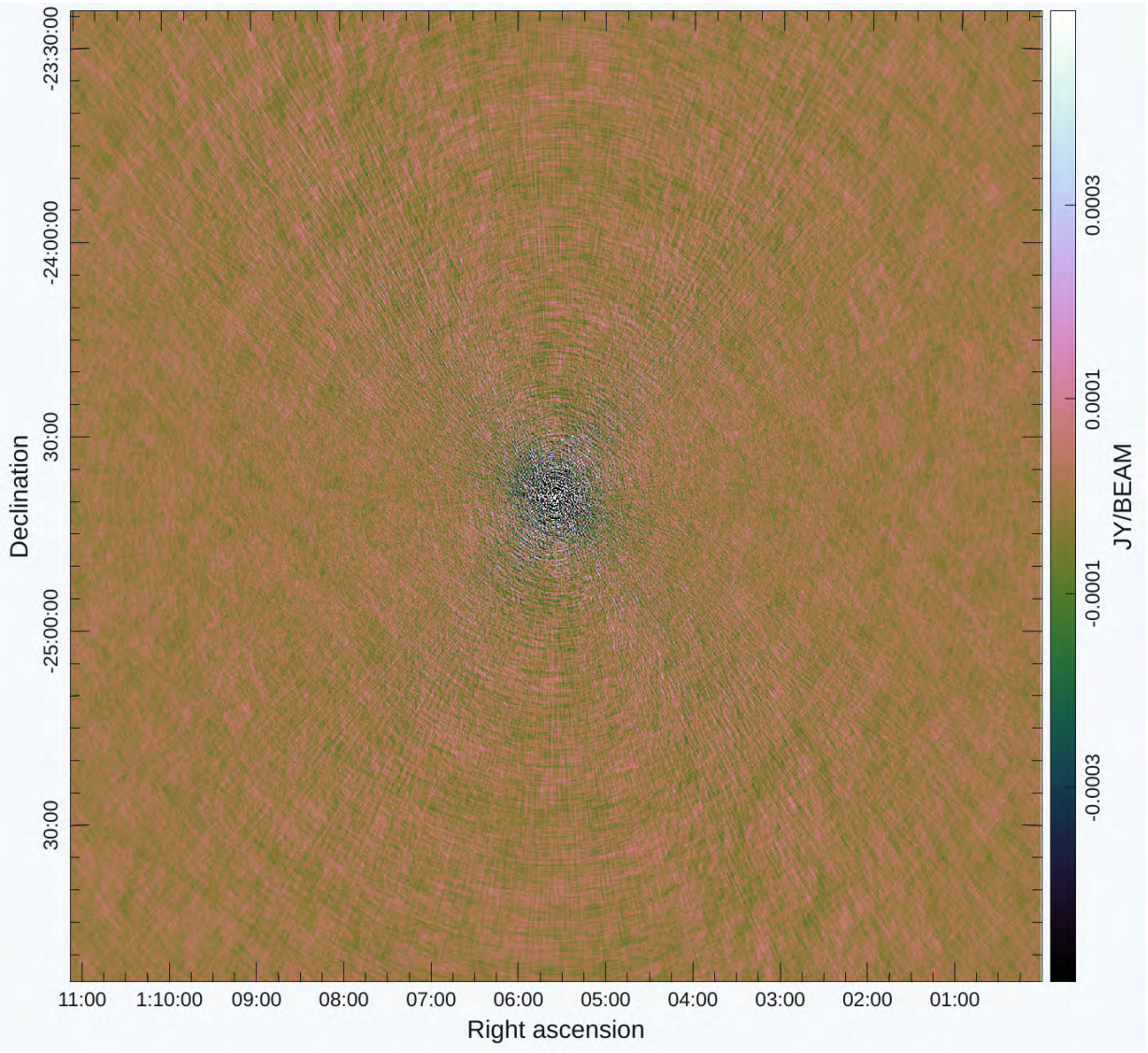

Figure 2.5: The PSF of our MeerKAT data.

5. repeat steps 1 through 4, where the residual image produced in step 4 becomes the dirty image in step 1. Repeat until a predetermined stopping criterion is reached. Common stopping criteria are a flux density threshold or a maximum number of iterations;

6. produce a *restored image*: this is obtained by convolving the model image with the CLEAN beam and adding it to the residual image. The CLEAN beam is obtained by fitting a two-dimensional Gaussian function to the PSF main lobe.

The CLEAN algorithm essentially treats the true sky to be a collection of independent pixels. In the case of point sources, this works well. However, in the case of extended, diffuse emission, the CLEAN algorithm will attempt to model the extended emission as several independent point sources. As a result, many variants of this algorithm exist, each with a different purpose.

The Cotton-Schwab (Schwab, 1984) algorithm is a variant of the CLEAN algorithm, though while the CLEAN algorithm is a model-fitting approach, the Cotton-Schwab algorithm implements a maximum entropy method, meaning that the Cotton-Schwab seeks an image that is consistent with the visibilities, but with maximum entropy. This involves finding the optimal solution while striking a balance between fitting to a model and over-fitting to a model. As such, this algorithm is ideal for extended diffuse emission.

Apart from deconvolution methods, several imaging options can be used in the process of forming the dirty image. We will illustrate three of them here that were used in the data reduction in this thesis work.

The Multi-Frequency Synthesis (MFS; Conway et al., 1990) algorithm takes advantage of the bandwidth to improve the u, v coverage. In the MFS algorithm, visibilities at each frequency are gridded separately and, as the u, v coordinates of each baseline change with frequency, this allows for improvement of the u, v coverage.

The imaging and deconvolution package used in this thesis is WSClean (Offringa et al., 2014), a fast implementation of a wide-field imager. WSClean allows for an `auto-cleaning` option as a stopping criterion for the Cotton-Schwab algorithm. Major iterations stop decon-

volving when the peak flux has reached the `-mgain` parameter (e.g., the flux has been reduced by 90% of its original brightness), and the entire deconvolution process will stop when the peak brightness reaches the criterion stipulated by the auto-threshold. Unlike an absolute threshold, auto-threshold will calculate the stopping threshold based on rms noise local to the source. As such, auto-threshold is more robust against calibration artefacts that may still be present in the image.

Finally, when baselines are gridded into a dirty image, they can be combined using different weights, a process often referred to as a *weighting* scheme. The most obvious weighting choice is the *natural weight*, where each u, v cell receives a weight proportional to the number of visibility measurements. The natural weighting scheme gives higher weight to short baselines compared to longer ones - as short baselines are always more numerous than longer ones in any array. This results in low angular resolution, but high brightness sensitivity. Conversely, the *uniform weighting* scheme gives equal weight to each u, v cell, regardless of the number of measured visibilities. This scheme effectively upweights long baselines with respect to short ones, sacrificing some sensitivity at the advantage of a better angular resolution.

A compromise between these two extremes is the Briggs (Briggs, 1995) weighting scheme, with a 'robust' parameter of 0, which allows for a trade-off between brightness sensitivity and angular resolution. The 'robust' parameter can be any number between -2 and 2, where -2 indicates a more uniform weighting, and 2 indicates a more natural weighting. An additional form of weighting, known as *tapering* can also be used. The most common taper used is a function of u, v length, in order to suppress either short or long baselines. In the analysis of diffuse emission, it is often necessary to increase surface brightness sensitivity by filtering out long baselines. This is done by applying a Gaussian taper *taper, T(u,v)*:

$$T(u, v) \propto e^{-\frac{u^2+v^2}{\sigma^2}}, \tag{2.15}$$

where σ is the taper width. Visibilities longer than σ are effectively downweighted in gridding.

2.4 Radio Interferometry Measurement Equation

Sky signals received by interferometers are always corrupted along their path.

First they can be corrupted by atmospheric/ionospheric effects. Variations in the number of electrons in the atmosphere and in the moisture levels of the troposphere can corrupt the sky signals (Brogan et al., 2018). The variation in the number of electrons in the atmosphere is due to terrestrial latitude, and can also vary according to the time of the year and the sunspot cycle (Thompson et al., 2017b). Finally, the electronic components of the receiving system can affect the signal.

It is assumed that the relationship between the true brightness and the visibilities is linear (Smirnov, 2011). That is, assuming an xyz coordinate system, where z is the line of propagation, an electromagnetic signal written in a matrix as,

$$\boldsymbol{e} = \begin{pmatrix} e_x \\ e_y \end{pmatrix} \tag{2.16}$$

that has undergone linear propagation effects, the signal received can be written as,

$$\mathbf{e}' = \begin{bmatrix} e'_x \\ e'_y \end{bmatrix} \tag{2.17}$$

where,

$$\mathbf{e}' = \mathbf{J}\mathbf{e} = \begin{bmatrix} j_{11} & j_{12} \\ j_{21} & j_{22} \end{bmatrix} \begin{bmatrix} e_x \\ e_y \end{bmatrix} \tag{2.18}$$

and $\mathbf{J}$ is a Jones matrix (Jones, 1942) . The Jones matrix is a complex, 2×2 matrix, which represents the cumulation of all the distortions affecting the original signal. This is possible as a linear transformation of a 2-element vector can be described by a 2x2 matrix. There is a Jones matrix for each linear transformation that the original signal undergoes, which are joined together to form a *Jones chain* (Smirnov, 2011). Matrices do not commute, and as such, the order of the Jones chain should be in the order in which the original electromagnetic signal is affected.

This generally results in the Jones chain of,

$$\mathbf{J} = \mathbf{GBDEKPZF} \tag{2.19}$$

where K-Jones is the geometric delay of the signal propagating through free-space; P-Jones is the parallactic angle rotation; Zeta-Jones is related to the population of electrons in the ionosphere; F-Jones is the Faraday rotation. The G-, B-, D-, and E-Jones matrices affect the signal once it has reached the telescope. The G-Jones is the electronic receiver gains, often split into two matrices, fluctuation as a function of frequency and time respectively. B-Jones, another electronic receiver gain, is the bandpass delay. E-Jones is the antenna's primary beam pattern sensitivity as a function of direction. Finally, D-Jones is the polarisation leakage experienced between two receivers.

The voltages measured by the antenna are a product of $\mathbf{J}$, and the original electromagnetic signal, $\mathbf{e}$,

$$\boldsymbol{v} = \begin{pmatrix} v_a \\ v_b \end{pmatrix} = \boldsymbol{J}\boldsymbol{e}. \tag{2.20}$$

To reconstruct the original EM signal, and thus the original sky model, the propagation effects represented by $\mathbf{J}$ must be accounted for. Some of these effects are well known, e.g the parallactic angle of rotation, while others need to be accounted for. Between a pair of antennas, there will be four voltage correlations, written as $\langle v_{pa} v_{qa}^* \rangle, \langle v_{pa} v_{qb}^* \rangle, \langle v_{pb} v_{qa}^* \rangle, \langle v_{pb} v_{qb}^* \rangle$, which can be arranged as in Smirnov, 2011 as,

$$V_{pq} = 2 \begin{pmatrix} \langle v_{pa} v_{qq}^c \rangle & \langle v_{pa} v_{qb}^* \rangle \\ \langle v_{pb} v_{qa}^* \rangle & \langle v_{pb} v_{qb}^z \rangle \end{pmatrix} = 2 \left\langle \begin{pmatrix} v_{pa} \\ v_{pb} \end{pmatrix} \left(v_{qa}^*, v_{qb}^* \right) \right\rangle = 2 \langle \boldsymbol{v}_p \boldsymbol{v}_q^H \rangle \tag{2.21}$$

where V_{pq} is known as the *visibility matrix*.When combining Eqn. 2.20 and 2.21, we will get,

$$\mathbf{V}_{pq} = 2 \left\langle \boldsymbol{J}_p \boldsymbol{e} \left(\boldsymbol{J}_q \boldsymbol{e} \right)^H \right\rangle = 2 \left\langle \boldsymbol{J}_p \left(\boldsymbol{e}\boldsymbol{e}^H \right) \boldsymbol{J}_q^H \right\rangle = 2 J_p \begin{pmatrix} \langle e_x e_x^* \rangle & \langle e_x e_y^* \rangle \\ \langle e_y e_x^* \rangle & \langle e_y e_y^* \rangle \end{pmatrix} J_q^H \tag{2.22}$$

where we can define the Brightness matrix, B as,

$$2 \begin{pmatrix} \langle e_x e_x^* \rangle & \langle e_x e_y^* \rangle \\ \langle e_y e_x^* \rangle & \langle e_y e_y^* \rangle \end{pmatrix} = B \tag{2.23}$$

as in Hamaker et al., 1996. Thus, the Radio Interferometry Measurement Equation (RIME) emerges,

$$V_{pq} = J_p B J_q^H \tag{2.24}$$

where V_{pq} is the visibility matrix, independent voltage vectors received and correlated by two antennas, p and q; B is the true sky brightness matrix; J_p and J_q^H are the Jones matrix. Equation 2.24 is the RIME based on the most simple case - a single, quasi-monochromatic source fixed at one point in the sky.

However, the observed sky is a continuous brightness distribution $B\,\hat{\sigma}$, where the unit direction vector is represented by $\hat{\sigma}$ (Smirnov, 2011). Such considerations lead to the full-sky RIME,

$$\mathrm{V}_{pq} = \boldsymbol{G}_p \left(\iint_{lm} \mathrm{E_p B E_q e}^{-2\pi i(u_{pq}l + v_{pq}m)} \mathrm{d}l\ \mathrm{d}m \right) \boldsymbol{G}_q^H, \tag{2.25}$$

where V_{pq} is the visibilities, and B is the true sky brightness, as in Eqn 2.24. G is the direction independent and E is the direction-dependent decomposition of the Jones matrix $J_p \times J_q^H$. When constructing the full-sky RIME, the visibilities need to be integrated over a sine projection of a unit sphere onto a plane (l, m), to accurately measure the visibilities over every possible direction (Smirnov, 2011).

2.5 First Generation Calibration

First Generation Calibration (1GC) is the process of solving for the Jones matrix in the RIME, in order to eventually recover the true sky brightness, or as close to it as possible. As discussed

previously, many factors can distort the visibilities; however, in practice, only the geometric, gain and bandpass delay are accounted for, as these are the fundamental factors. Thus we impose,

$$\vec{J} = KGB \tag{2.26}$$

where G is the gain, K is the delay error, and B is the bandpass error. To eventually calibrate the target visibilities, we observe well-known, point-like sources, known as calibrator sources. The calibrator sources are observed intermittently with the target field, the calibration process finds the solution for each antenna pair, and finally, those solutions are applied to the target visibilities.

Gain Calibration

The time variable gain, or simply the gain, is the amplitude and phase component. The amplitude is affected by the electronic component of the antenna, and as such usually is stable; the phase is affected by both the electronic components as well as the atmospheric effect. As a result, it is imperative that the complex gain solutions, G_i and G_j, where *i* and *j* represent an antenna, are calculated and applied to the measured visibilities, V_{ij}^m, to produce meaningful, calibrated visibilities, V_{ij}^c, as such,

$$V_{ij}^c = \frac{G_i^* \cdot G_j}{|G_i| \cdot |G_j|} V_{ij}^m \tag{2.27}$$

The corrections are derived through 1GC, by comparing the known values of the calibrator source's measured visibilities to that of that target's measured visibilities. The gain is best solved over large frequency intervals and small time scales, indicating that the gain calibrator source must be observed frequently, for short time scales. By following the gain calibrator, atmospheric effects affecting the target will also be captured. Thus, the calibrator source must be near the target source; however, the gain calibrator need not be bright, nor is it necessary to know the flux of the source.

Bandpass Calibration

An interferometer might not be equally sensitive across all frequencies. This is known as a bandpass error, denoted by a B-Jones matrix, where

$$B = B(\nu) \tag{2.28}$$

The bandpass comes from the electronic receivers, indicating that it should be stable with respect to time. When solving for the B-Jones matrix, the best calibrator source to observe would be a bright, well-known source, as the amplitude and phase components would be well-known. The calibrator source does not necessarily need to be near to the target.

Delay Calibration

The delay error is denoted by a K-Jones matrix, where

$$K = e^{i\delta(t)\nu}. \tag{2.29}$$

Delay errors are caused by any factor that could potentially delay a signal as it travels from the source to the interferometer, causing a difference in path length. Such causes could be atmospheric or instrumental. Atmospheric effects that result in gain fluctuations can be dominated by the variations of electron content in the ionosphere, as well as the fluctuation in water content of the troposphere. The former is more prevalent at lower frequencies, while the latter is rampant at higher frequencies (Brogan et al., 2018).

2.6 Second Generation Calibration

Post-1GC, the images produced will still contain calibration and imaging artefacts. This is only problematic if the artefacts interfere with the target, as is often the case. The solution to this problem is *self-calibration*. As calibration sources are used to solve for gain solutions in 1GC,

self-calibration, or second-generation calibration (2GC) is the process of using the target field to further derive gain solutions, thus reducing the imaging and calibration artefacts. 2GC is a cyclical process, where each iteration of the process should improve the image of the target field.

The process of self-calibration will typically use imaging software (in this thesis, we use WSClean, Offringa et al. (2014)) and calibration software (in this thesis, we use CubiCal, (Kenyon et al., 2018)). The process can be described by the following procedure:

1. the best sky image, probably featuring some artefacts, is used to derive a sky model. This is done by detecting the brightest pixels in the sky, and populating the data set with this model. This is stored in the *'model data'* column of the measurement set (the data format adopted by CASA).

2. from the sky model, a mask is made. A mask is used to exclude bright sources in the cleaning process to allow for a deeper clean, often beyond the noise level, which in turn will allow for deeper deconvolution.

3. with the mask in place, a new image is produced, and as such, a new sky model will populate the model column in the measurement set.

4. visibilities in the new image are processed by calibration software, which fits the visibilities to the model data, and flags any detected errors. This fitted, flagged data is recorded in the measurement set, populating the *corrected-data* column, concluding the first iteration of self-calibration.

Usually, several iterations are required for self-calibration, where the solution intervals for each iteration decrease. Generally, the self-calibration process is ended when the improvemnt in the images becomes nominal.

Several tools have been developed to aid in the reduction of iterations necessary for self-calibration, one of which is `auto-mask` in WSClean. An essential step in self-calibration is having an adequate mask, which requires a somewhat complete sky model image. A good sky

model is often not available, as a dirty image generally does not have a sufficient sky model, due to the potential artefacts still present, and particularly when there are bad gain solutions present. Making use of `auto-mask` in WSClean can mitigate this issue. After creating an initial image, `auto-mask` detects bright sources above a supplied threshold and creates a mask to clean around, which will improve the cleaning. Each iteration of imaging updates the model column in the measurement set, thus improving the sky model used for auto-masking. Once artefacts have been sufficiently suppressed, a more detailed mask can be made.

CHAPTER 3

Observations and Data Reduction

3.1 Observations

Observations for this project include the target galaxy cluster A 141, as well as three calibrators (Table 3.1). They took place on May 15^{th} 2021 and April 5^{th} 2021, respectively, using the MeerKAT L-band receiver at a central frequency of 1283 MHz, with an 856 MHz bandwidth. The observing setup includes 4096 channels with a channel width of 208.98 kHz and a 4 s integration.

The target was observed for 5 hours in each observing run, with the primary calibrator, J0408-6545, being observed for 10 minutes every three hours, and the secondary calibrator, J0025-2602, being observed for 2 minutes every 40 minutes, approximately. The polarisation calibrator, J0137+3309, was also observed twice, for an exposure time of 5 minutes. It is important to note that, throughout this thesis, we have adopted a standard cosmology, with

Object Name	RA	DEC
A 141	$01^{\mathrm{h}}\,05^{\mathrm{m}}\,34.15^{\mathrm{s}}$	$-24^{\circ}\,39'\,34.0''$
J0408-6545	$04^{\mathrm{h}}\,08^{\mathrm{m}}\,20.38^{\mathrm{s}}$	$-65^{\circ}45'\,09.1''$
J0025-2602	$00^{\mathrm{h}}\,25^{\mathrm{m}}49.16^{\mathrm{s}}$	$-26^{\circ}\,02'\,12.6''$
J0137+3309	$01^{\mathrm{h}}\,37^{\mathrm{m}}\,41.3^{\mathrm{s}}$	$+33^{\circ}\,09'\,35.1''$

Table 3.1: Coordinates of target and calibrator sources.

$H_0 = 69.6$ km s^{-1}Mpc^{-1}, $\Omega_M = 0.286$, $\Omega_\lambda = 0.714$ (Planck Collaboration et al., 2020). As such, at at the cluster redshift $z = 0.23$, $1''$ subtends a 3.704 kpc linear scale.

3.2 Data Reduction

Most of the data reduction is carried out using the Containerized Automated Radio Astronomy Calibration (CARACal; Józsa et al., 2020, CARACAL;) pipeline, which uses the Common Astronomy Software Applications (CASA; McMullin et al., 2007) to automate the 1GC and 2GC procedures, as well as CubiCAL (Kenyon et al., 2018), a calibration suite that offers a fast implementation of interferometric calibration algorithms. The data set is first averaged over frequency and time; the 4094 channels are averaged to 1024 channels, and the 2s integration interval is averaged to 8s. CARACal operates through a configuration script that runs each step of the data reduction pipeline. The default MeerKAT continuum pipeline [1] is used and adapted as needed. CARACal first separates the measurement sets into target and calibrator measurement sets, then begins with flagging the calibrator data measurement set.

When flagging the calibrator measurement set, we make use of multiple flagging strategies. Firstly, we use an RFI mask [2] designed specifically for MeerKAT observations; the mask excludes all the channels within the MeerKAT observing bands known to be affected by RFI.

[1] https://github.com/caracal-pipeline/caracal/blob/master/caracal/sample_configurations/meerkat-continuum-defaults.yml

[2] caracal/data/meerkat_files/meerkat.rfimask.npy

Secondly, we flagged additional well-known problematic ranges of the spectral window ($856-880$ MHz, $1658-1800$ MHz, and $1419.8-1421.3$ MHz), as well as shadowed antennas. Finally, we make use of a data processing flagging code, known as Tricolour RFI flagger (Hugo et al., 2022), which is specifically designed for MeerKAT observations. Tricolour has several flagging strategies, each varying in strictness. We adopted a stringent Tricolour flagging strategy [3] to ensure the cleanest possible data.

As discussed in Section 2.5, the process of 1GC requires observing well-known calibrator sources, solving for instrumental gains and, subsequently, applying the gain solutions to the target data - a process sometimes referred to as *cross-calibration*. After flagging, we use the CARACal default parameters to proceed with cross-calibration. The primary calibrator is used to solve for instrumental delays and the bandpass. The primary calibrator is assumed to be 22.4 Jy at 1.0 GHz with a spectral index $\alpha = -1.12$ [4]. Delay and bandpass solutions are then applied to the secondary calibrator, which is used to solve for delays and complex gains as a function of time, using a 4 s interval. We apply the calibration solutions obtained from the primary and secondary calibrators to the galaxy cluster target. The calibrated visibilities are Fourier transformed into a *dirty image* using WSClean (Offringa et al., 2014). We use a Briggs (Briggs, 1995) weighting scheme, with a robustness parameter of zero. This weighting is a compromise between side-lobe suppression that would be achieved using uniform weighting, and optimal noise that would be achieved using natural weighting, allowing for the best trade-off between angular resolution and brightness sensitivity.

We deconvolve the dirty image using the Cotton-Schwab (Schwab, 1984) algorithm. We use the WSClean auto-threshold option, which sets the deconvolution threshold according to the noise rms locally to the detected source. Compared to the standard deconvolution threshold, which is set to be constant across the image, the auto-threshold choice is generally more robust

[3] https://github.com/caracal-pipeline/caracal/blob/master/caracal/data/meerkat_files/khruschev.yaml

[4] https://skaafrica.atlassian.net/wiki/spaces/ESDKB/pages/1481408634/Flux+and+bandpass+calibrationJ0408-6545

against calibration artefacts that may still be present in the image. We set the auto-threshold to be three times the local noise rms. Additionally, we used the auto-masking option in WSClean, where a mask is automatically generated around each detected source to constrain the search for clean components that describe the source.

The deconvolved image is shown in Figure 3.1, where artefacts are still visible around the brightest sources and calibration errors still limit the detectability of diffuse emission associated with the cluster (see also Figure 3.2 for a zoom-in).

We improve the image quality through self-calibration, again using CARACal. CARACal employs Cubical for self-calibration. We use the model produced during the deconvolution process, which includes all the compact sources brighter than 80 μJy. We perform four consecutive rounds of self-calibration where we start with a 10-minute solution interval and then decrease it to 2 minutes, 1 minute and 20 seconds respectively. An image is made after each self-calibration iteration, improving the sky model through a deeper deconvolution. The deconvolution threshold is set automatically by the auto-threshold and auto-mask options. The resulting image after four rounds of self-calibration can be seen in Figure 3.3.

Self-calibration significantly improves the image fidelity (see Figure 3.4) and, consequently, the image noise from 13.9 μJy beam^{-1} before self-calibration to 9.38 μJy beam^{-1} after self-calibration. Some artefacts, however, still remain in the image, particularly a stripy pattern that runs across the whole image and that was not corrected by self-calibration, likely caused by phase solutions that did not converge at some time intervals. We derive the deepest sky model possible from Figure 3.3 by masking all the emission below 58 μJy. We use the Breizorro software (Ramaila et al., 2023). Breizorro is an efficient mask-making tool that creates a noise map of an input image, applies a threshold specified by the user to the noise map, then sets each pixel of the noise map to be 1 if the pixel is greater than the threshold, and 0 if it is not, thus creating a binary mask.

We identify bad gain solutions as outliers in the gain solutions as a function of time (see Fig-

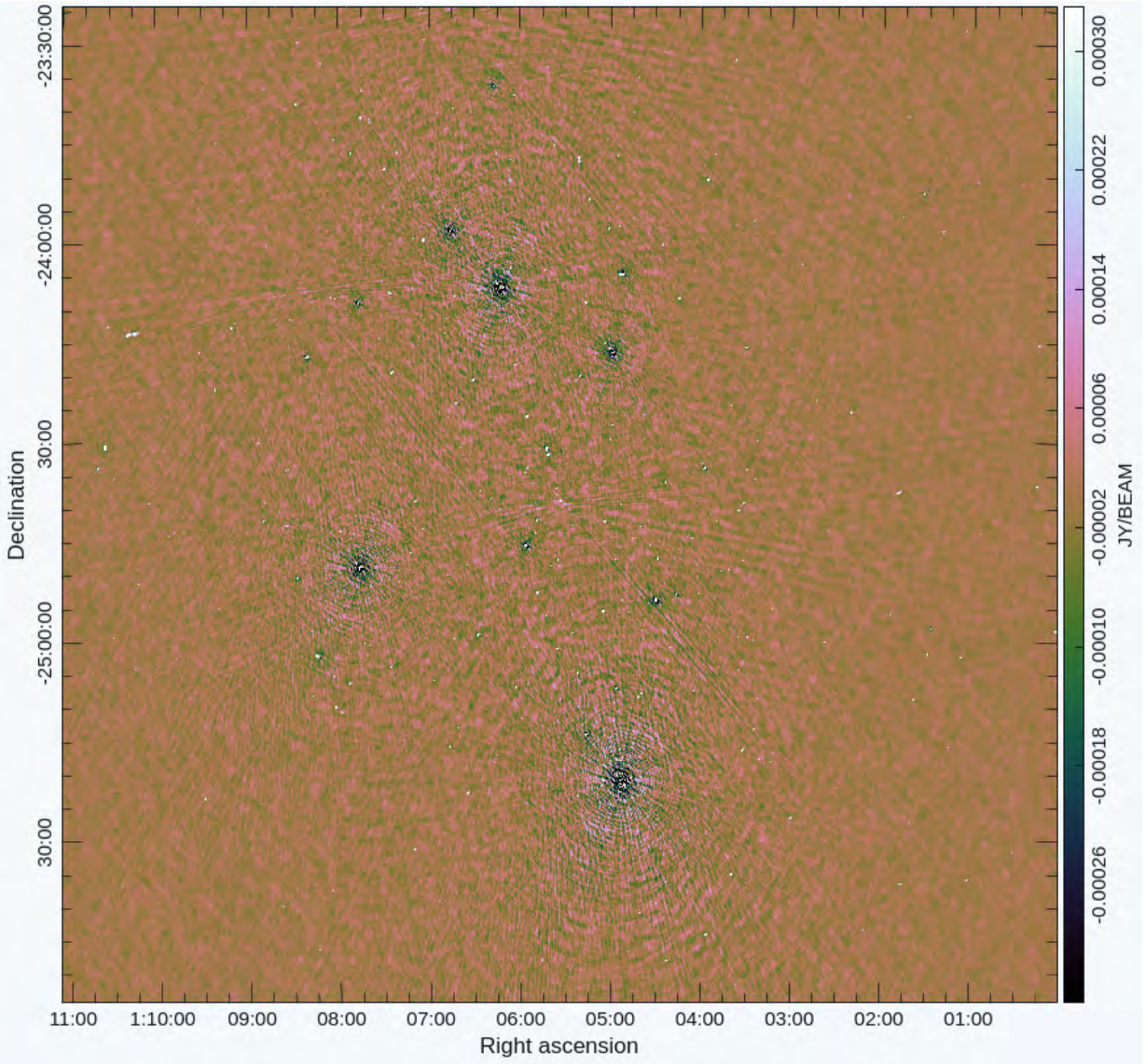

Figure 3.1: MeerKAT image of the A 141 field at 1.28 GHz. The image covers approximately the MeerKAT primary beam and has a 13.9 μJy beam^{-1} noise rms. Its angular resolution is $6.6'' \times 5.6''$.

Figure 3.2: Zoom into Figure 3.1, at the cluster location. Calibration and deconvolution limitations still prevent a clear detection of diffuse emission associated with the cluster.

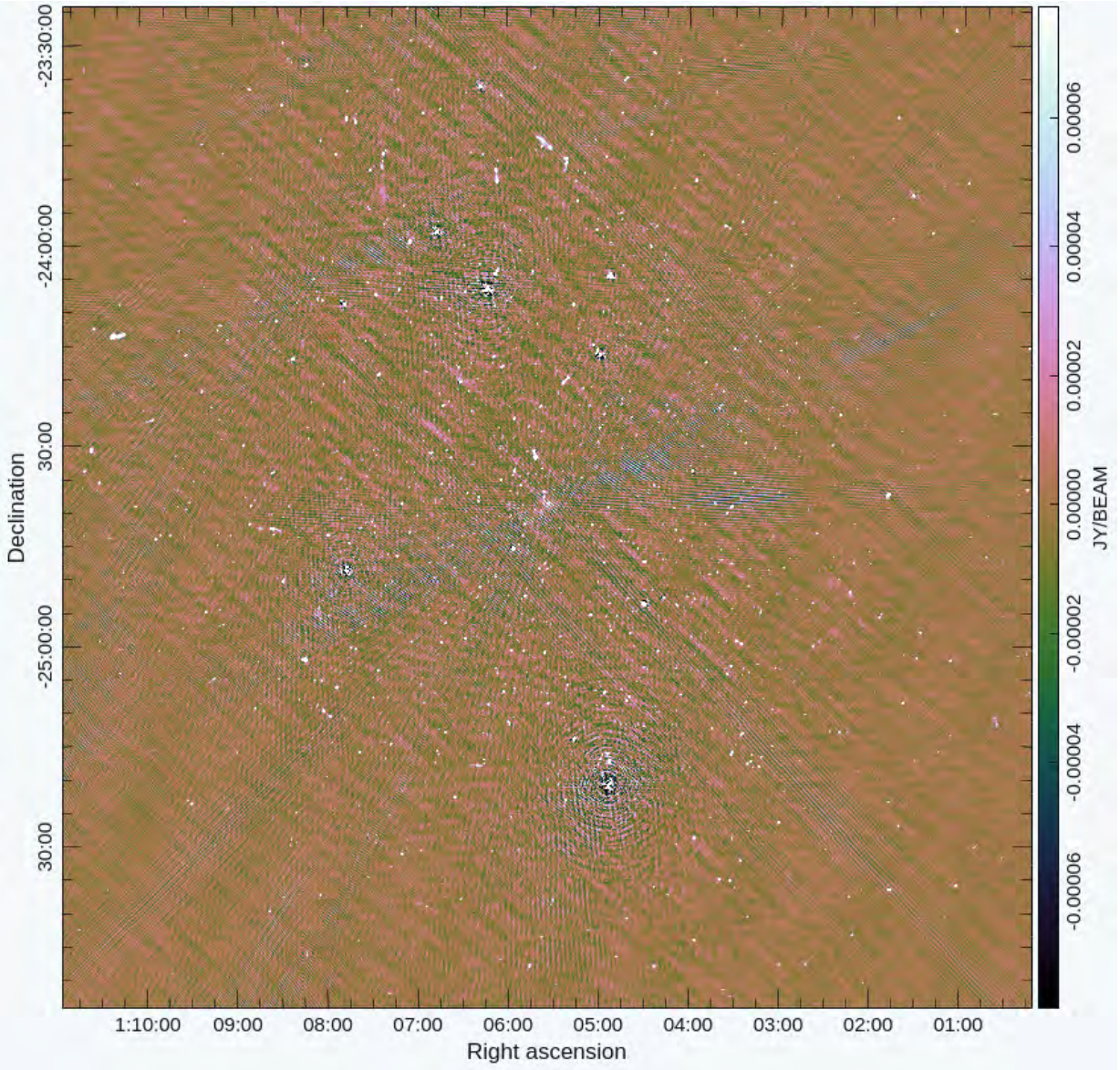

Figure 3.3: The A 141 field after four rounds of self-calibration. The image has 9.38 μJy beam^{-1} noise rms and a $7.8'' \times 6.6''$ angular resolution. A residual, stripy pattern of systematic effects is still visible across the image.

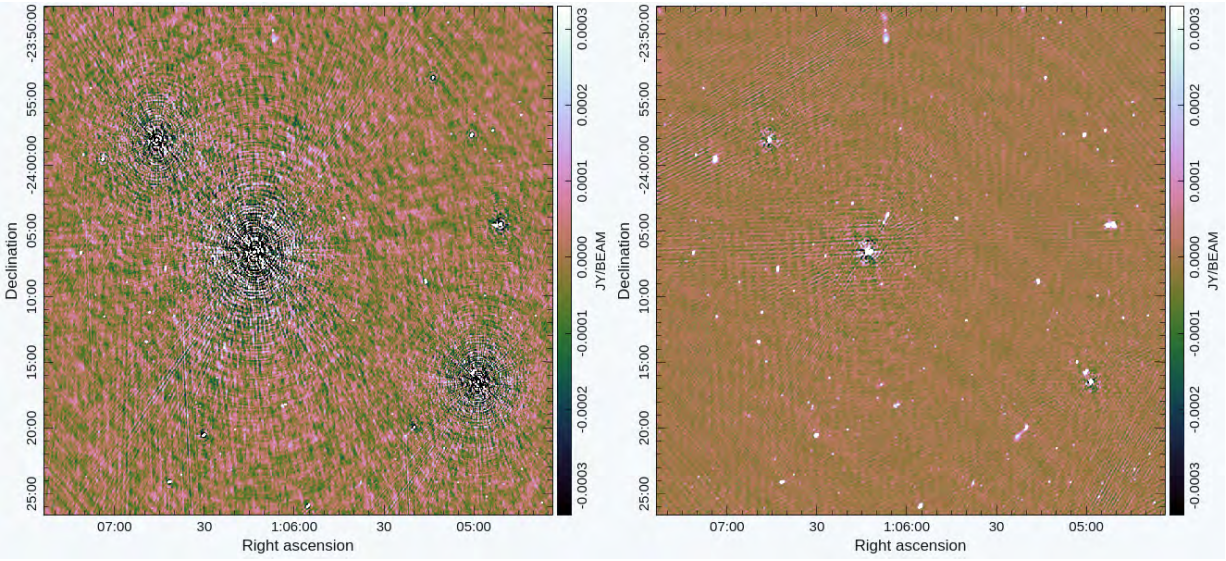

Figure 3.4: Image details before (left) and after (right panel) self-calibration. Artefacts around bright sources are clearly suppressed by self-calibration. The noise improves from 13.9 μJy beam^{-1} to 9.4 μJy beam^{-1}.

ure 3.5) and flag them accordingly. This only partially removes the artefacts from the image and in order to identify the bad scan/baselines, we proceed to Fourier transform the residual image after subtracting the best sky model available. The Fourier-transformed residual image clearly shows bright pixels, with a pattern that is not similar to sky-like emission and is indicative of calibration errors. We identify the visibilities corresponding to the bright pixels in Figure 3.6 and flag them. We obtain a final image that is virtually free of artefacts, apart from a few residual errors around the four brightest sources. Correcting these errors would require the implementation of direction-dependent calibration, however, these errors do not significantly affect the central portion of the image, where the cluster is located (Figure 3.7).

Figure 3.7 is made using a Briggs weighting scheme with a robust parameter equal to zero, in order to achieve a trade-off between surface brightness sensitivity and angular resolution. Diffuse emission is visible at the cluster location (Figure 3.8), still contaminated, however, by a certain number of point sources. In order to remove the point source contribution and highlight the diffuse emission, we create a uniform-weighted, high-resolution image where diffuse emission

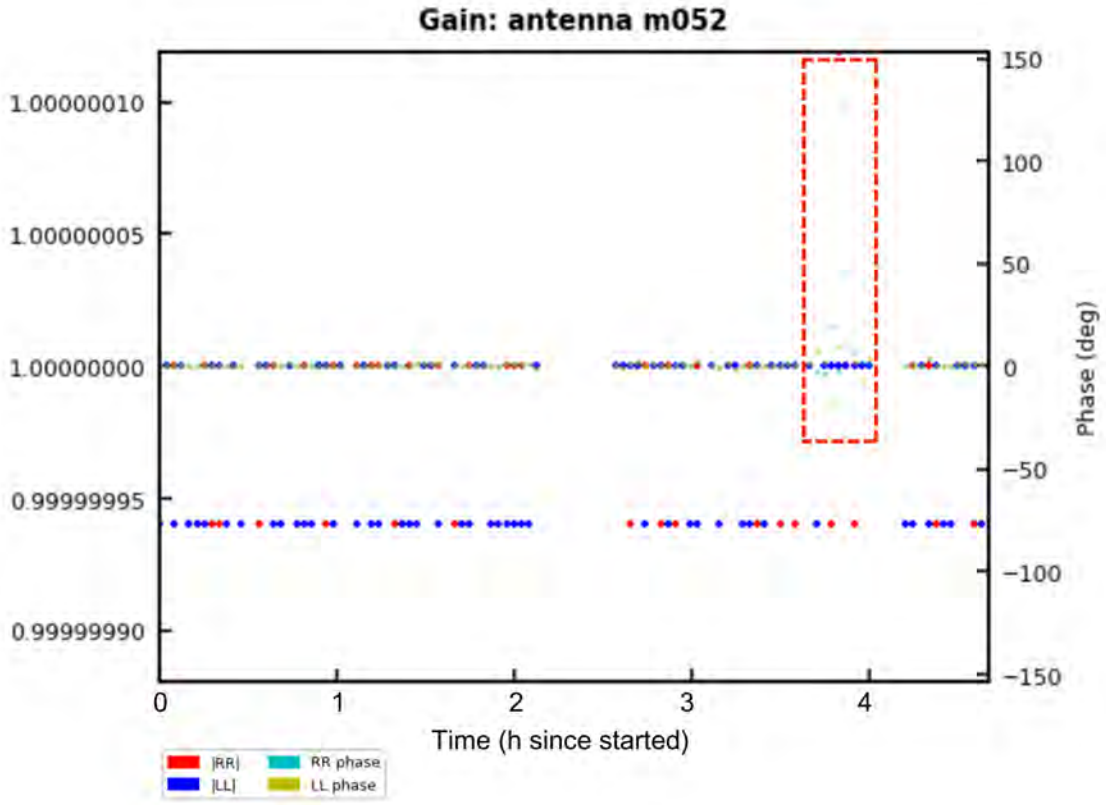

Figure 3.5: Plot of gain solutions for one antenna in the second measurement set. The gain solutions in the red dashed box indicate bad gain solutions.

is hardly visible (Figure 3.9). We use this image to create a final Breizorro mask. We model all the sources brighter than 60 μJy beam^{-1} and subtract them from the visibilities in order to obtain a residual image (Figure 3.10). This subtraction results in a residual image that is virtually featureless. We, therefore, proceed to create a residual image at a coarser resolution, where the diffuse emission at the cluster location is clearly visible (Figure 3.11). We make use of the final Breizorro mask to clean this image down to 7.01 μJy.

The coarser resolution is achieved by applying a Gaussian taper (recall Equation 2.15) of $15''$ using WSClean, which resizes the restoring beam to be around $15'' \times 15''$. Additionally, a Briggs weighting equal to 0.25 is used to enhance the diffuse emission.

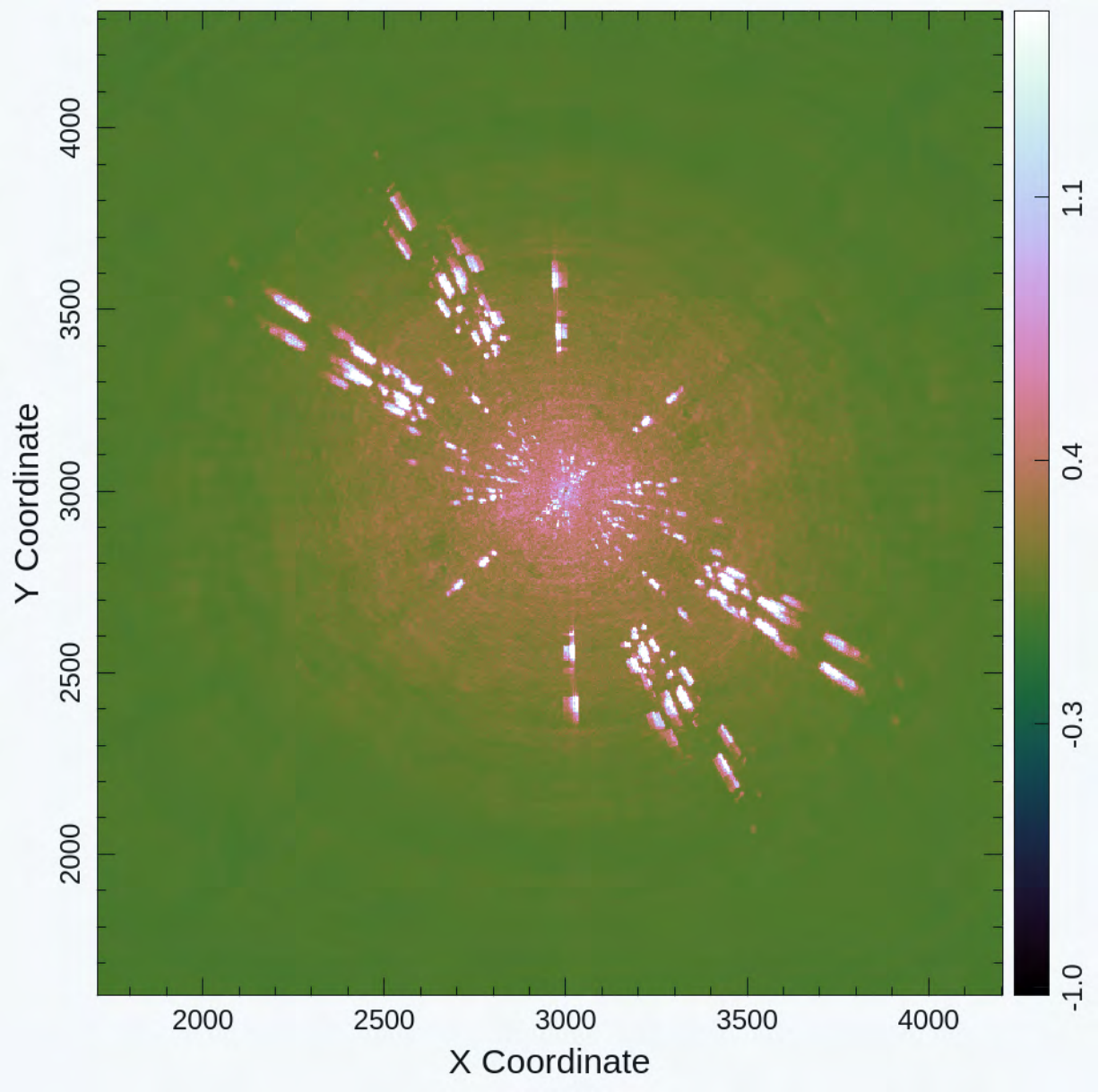

Figure 3.6: Fourier transform of the residual image. Bright pixels denote calibration errors that are responsible for the ripple pattern visible in Figure 3.3.

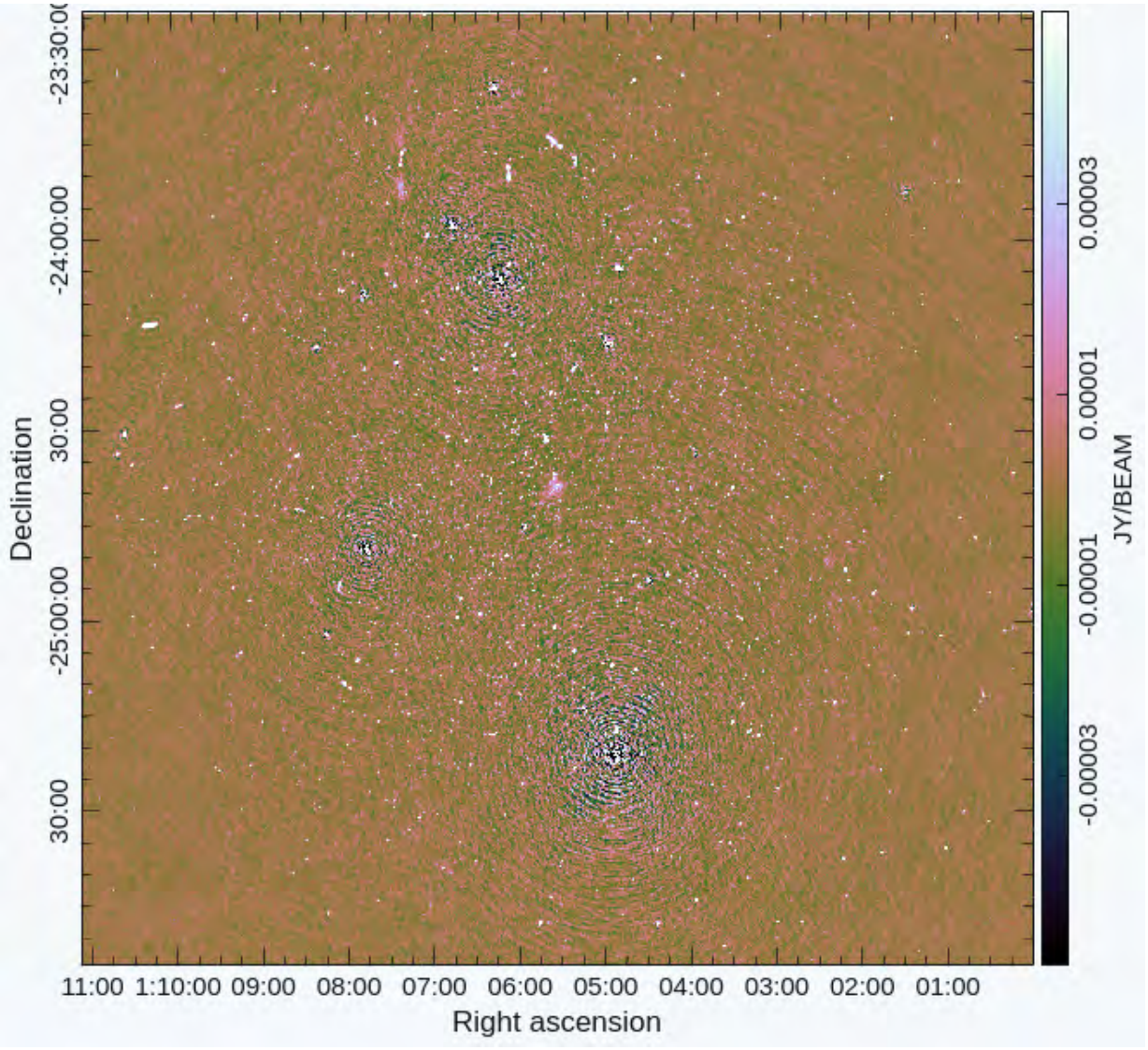

Figure 3.7: The A 141 field after self-calibration. The noise rms is 4.3 μJy beam^{-1}, and the angular resolution is $7.7'' \times 6.6''$. We note that a few sources still show calibration artefacts that, however, do not affect the image at the cluster location.

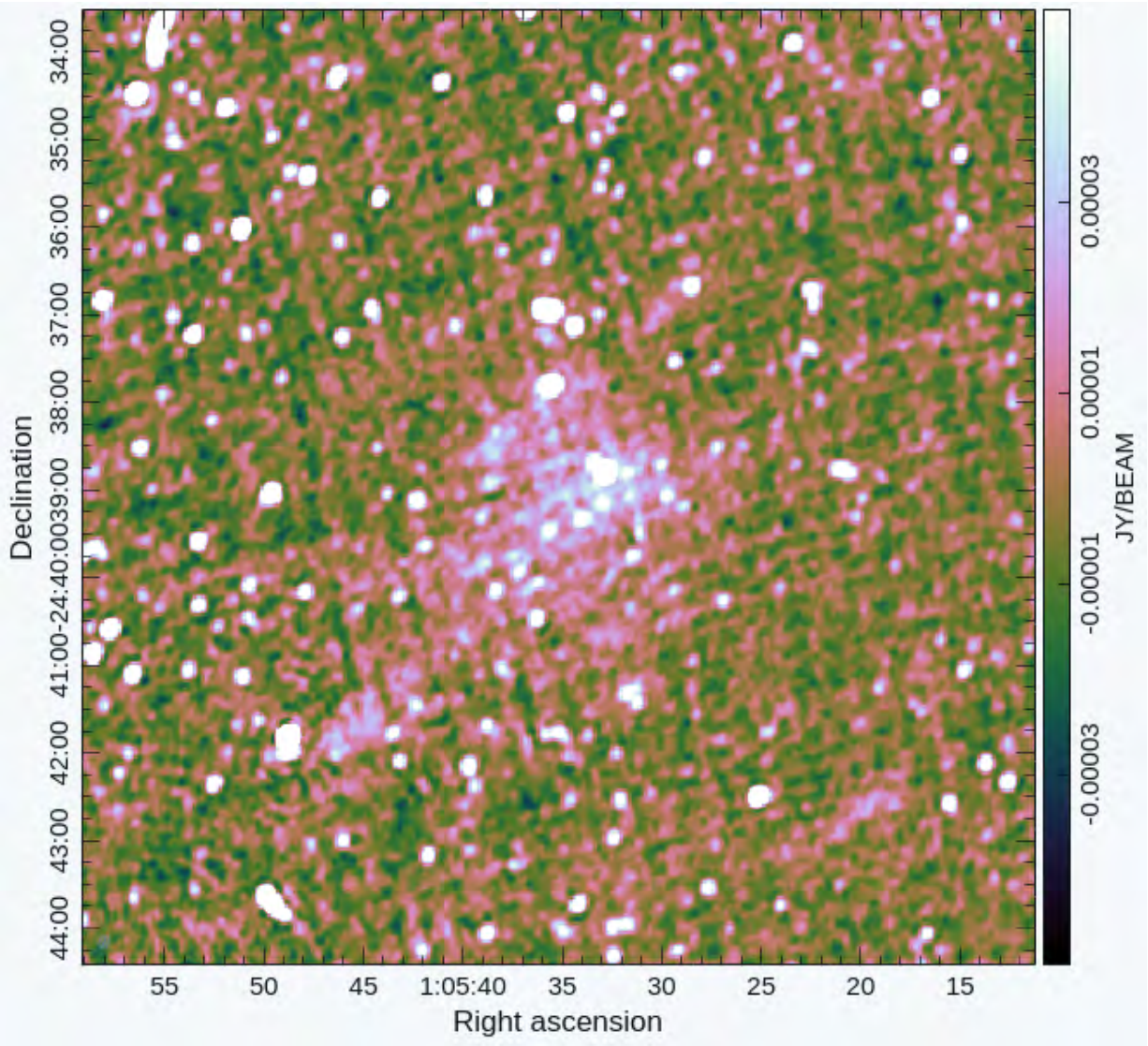

Figure 3.8: Figure 3.7, zoomed into the cluster centre. The noise rms is 4.3 μJy beam^{-1}, and the angular resolution is $7.7'' \times 6.6''$. Diffuse emission is visible at the cluster location.

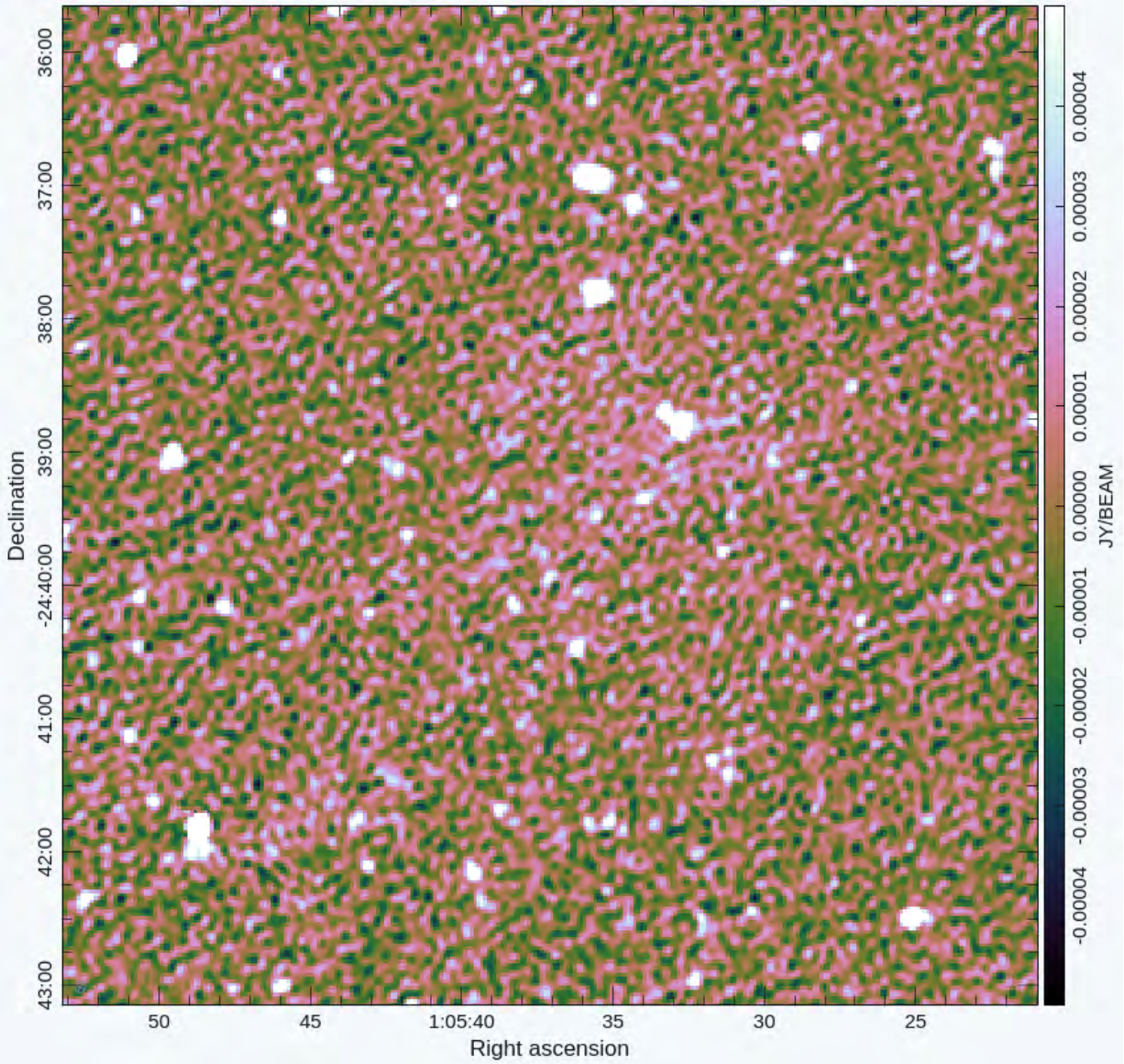

Figure 3.9: Uniform weighted restored image, zoomed at the cluster position. The noise rms is 9.0 μJy beam^{-1}, and the angular resolution is $5.1'' \times 4.4''$. As expected, the diffuse emission is almost completely suppressed by the uniform weighting scheme.

Figure 3.10: Uniform weighted residual image, zoomed at the cluster position. The noise rms is 9.0 μJy beam^{-1}, and the angular resolution is $5.1'' \times 4.4''$. Compared with Figure 3.9, we can see that sources were subtracted accurately, without any apparent residual error, leaving a fairly uniform residual across the image.

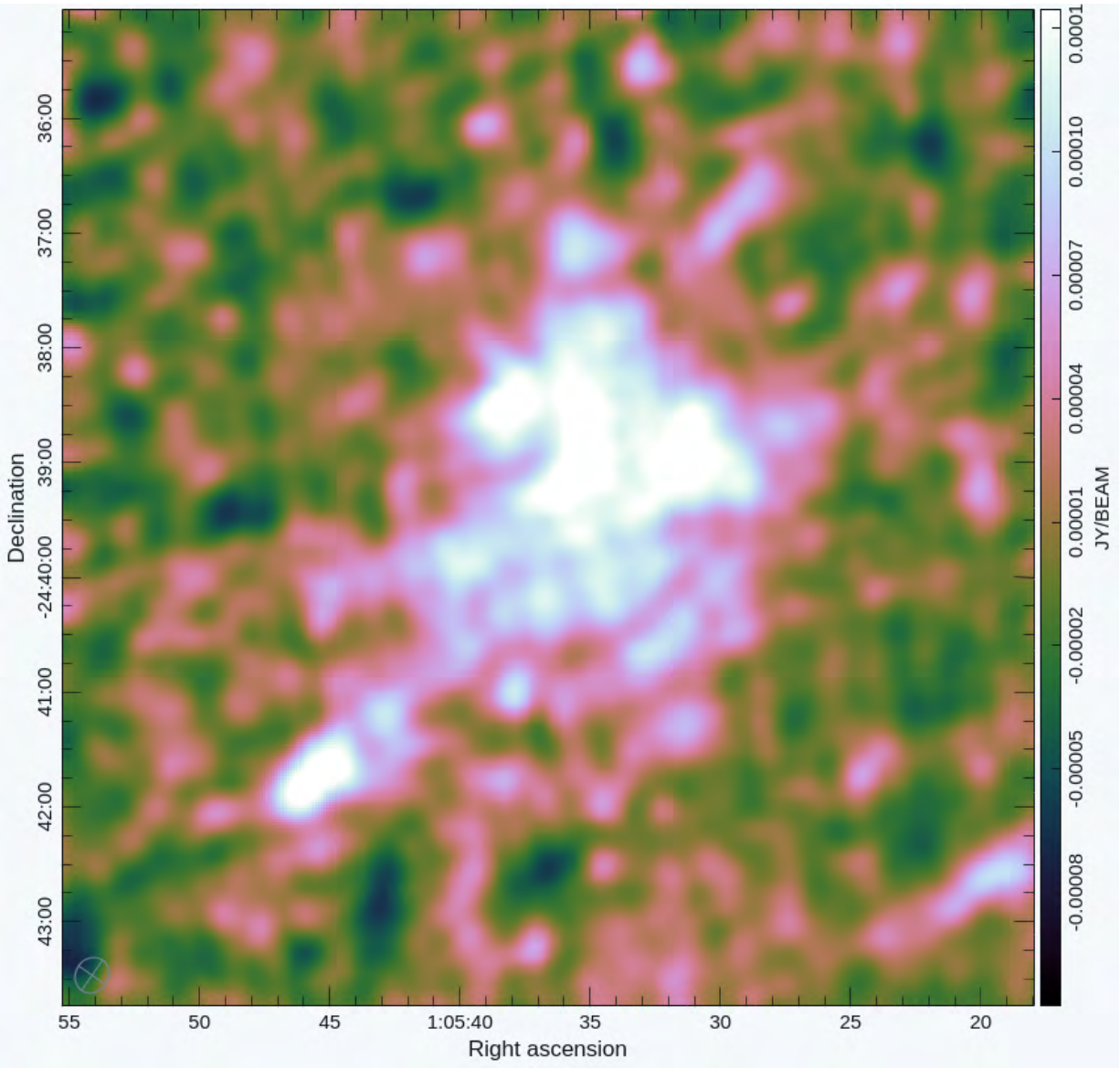

Figure 3.11: Briggs 0.25 weighted image, with a $15''$ taper applied and after compact sources were subtracted. The noise rms is 8.8 μJy beam^{-1} and the restoring beam is $19'' \times 17''$.

CHAPTER 4

Results and Discussion

In the previous chapter, we present the source-subtracted, $19'' \times 17''$ resolution image (Figure 3.11) that shows significant diffuse emission at the centre of the galaxy cluster A 141, well above the 3σ contours, with a 10 mJy beam^{-1} peak surface brightness. Figure 4.1 compares the diffuse emission from our $19'' \times 17''$, 1.28 GHz MeerKAT image to the $49'' \times 46''$, 943.5 MHz ASKAP image (Duchesne et al., 2021). We achieve a surface brightness sensitivity that is ~ 2.3 deeper than the ASKAP image, at an improved resolution. The diffuse emission detected at 1.28 GHz has a morphology similar to the image at 943 MHz (Duchesne et al., 2021). We measured the maximum and minimum extension of the diffuse emission, (excluding the South-East peripheral structure) to be $4.4' \times 3.9'$ arcmin, corresponding to a linear size of $\sim 970 \times \sim 860$ kpc respectively. The South-East peripheral structure has a maximum extension of 2.2', corresponding to a linear size of ~ 490 kpc.

Figure 4.2 compares the X-ray and 1.28 GHz emission, showing a clear overlap of the North-

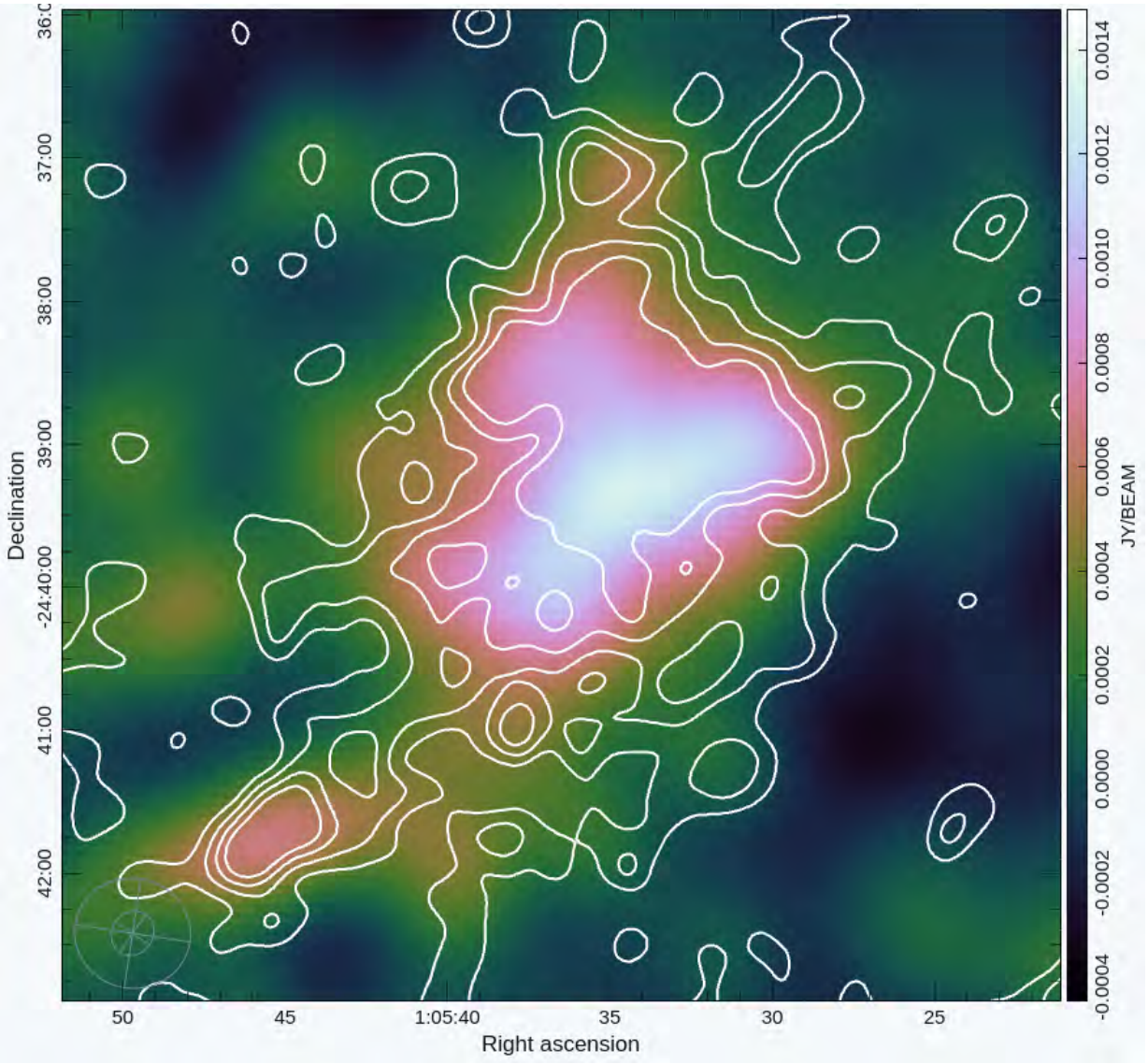

Figure 4.1: A 141 image at 943.5 MHz with a $49'' \times 46''$ resolution, and a 140 μJy beam^{-1} noise rms (ASKAP, Duchesne et al., 2021). Contours are overlaid from the source subtracted, low-resolution MeerKAT image (Figure 3.11). Contours are drawn at 3, 6, 9 and 12σ (where σ is 8.8 μJy beam^{-1}).

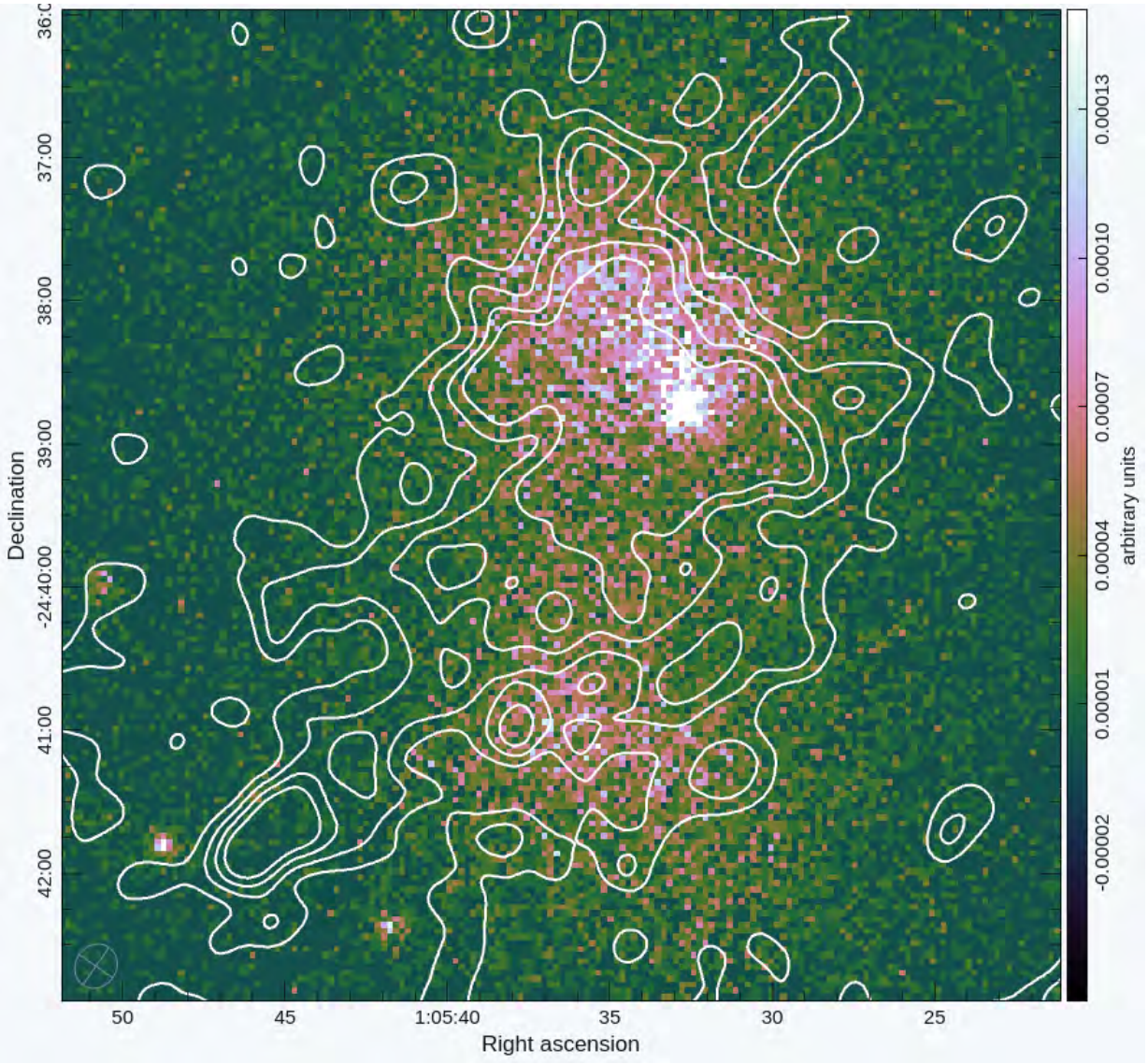

Figure 4.2: XMM-Newton image showing the emission corresponding to the two subclusters, as well as the connecting region. Contours are overlaid from the source subtracted, low-resolution MeerKAT image (Figure 3.11) and drawn at 3, 6, 9 and 12σ (where σ is 8.8 μJy beam^{-1}).

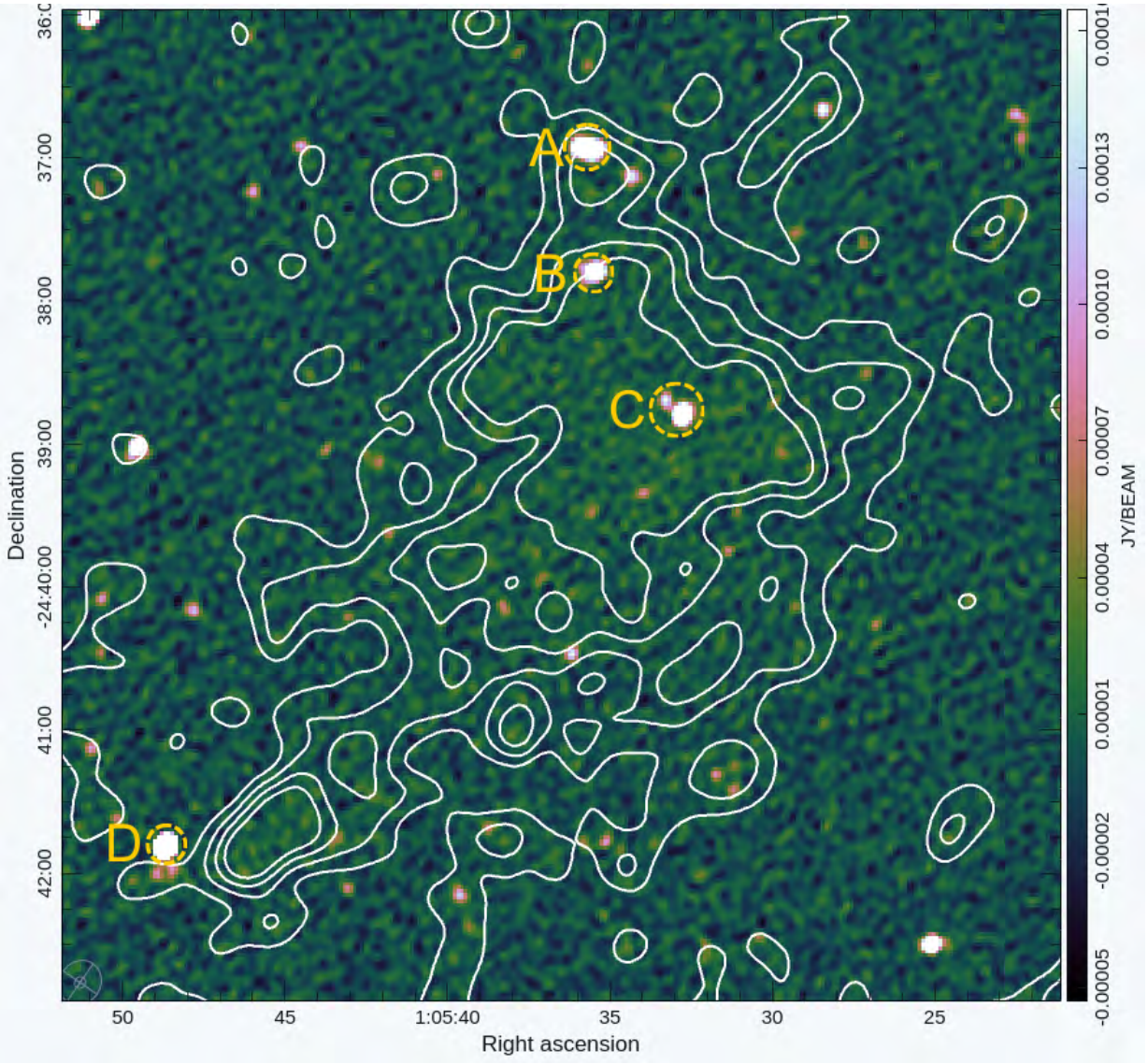

Figure 4.3: MeerKAT image at 1.28 GHz with a 9 μJy beam^{-1} noise rms and a $5.1'' \times 4.4''$ angular resolution (same as Figure 3.9). We labeled the same point sources detected at 943 MHz same as Duchesne et al. (2021). Contours are overlaid from the source subtracted, low-resolution image (Figure 3.11) and are drawn at 3σ, 6σ, 9σ, and 12σ (where σ is 8.8 μJy beam^{-1}).

ern subcluster between them. We notice, however, a displacement towards South, of $\sim 1'$, between the peak of the X-ray and radio emission respectively. The co-location between X-ray and radio emission, confirmed by both the 943 MHz and the higher-resolution 1.28 GHz image definitely indicates the presence of a radio halo associated with A 141. The radio emission, however, extends well beyond the X-ray emission associated with the North subcluster, covering the entire Southern subcluster, too. However, there is no visible increase in the radio surface brightness corresponding to the peak X-ray emission associated with the Southern subcluster.

Radio emission overlaps with the bridge of X-ray emission between the two subclusters, although it does not accurately match the X-ray morphology. Like the 943 MHz emission, the radio emission at 1.28 GHz extends towards the South-East beyond the X-ray emission, and towards one of the subtracted radio sources, namely source D, according to the labelling by (Duchesne et al., 2021, see Figure 4.3). The 943 MHz image by Duchesne et al. (2021) does not have sufficient angular resolution to clearly distinguish the peripheral South-East structure from the rest of the halo but our observations clearly do.

We measured the flux density of the entire diffuse emission at 1.28 GHz (i.e, the halo and South-East peripheral structure) by integrating above the 3σ contours, obtaining $S_{1.28} = 10.8 \pm 0.3$ mJy. The uncertainty was computed as (e.g., Cassano et al., 2013):

$$\sigma_{f_H} = \sqrt{(\delta_{\rm cal} f_H)^2 + \left(\sigma\sqrt{N_{\rm beam}}\right)^2}, \tag{4.1}$$

where f_H is the integrated halo flux density; $\delta_{\rm cal}$ is the uncertainty of the flux calibrator, expressed as a percentage; N_{beam} is the number of independent beams that cover the area of the diffuse emission. In our case $\delta_{\rm cal} = 3\%$, $N_{\rm beams} = 167$ and $\sigma = 8.8$ μJy beam^{-1}. The flux density of the South-East peripheral source and the radio halo are found to be $S_{\rm ph} = 1.2 \pm 0.2$ mJy and $S_{\rm h} = 9.6 \pm 0.3$ mJy respectively.

We use the spectral index, $\alpha = -1.06 \pm 0.09$, as reported in Duchesne et al. (2021), to scale the integrated flux density to 943.5 MHz, finding $S_{943\ \rm MHz}$ as:

$$S_{943\ \rm MHz} = S_{1.28\ \rm GHz}\left(\frac{1.28\ \rm GHz}{0.9435\ \rm GHz}\right)^{\alpha}, \tag{4.2}$$

finding $S_{943\ \mathrm{MHz}} = 14.9 \pm 0.6$ mJy, consistent with the value reported by Duchesne et al. (2021), 13.7 ± 1.9 mJy. The error on the flux density scaled to 943.5 MHz was calculated using the standard error propagation:

$$\Delta S_{943.5\ \mathrm{MHz}} = \sqrt{\left(\frac{\partial S_{943\ \mathrm{MHz}}}{\partial S_{1.28\ \mathrm{GHz}}}\right)^2 (\Delta S_{1.28\ \mathrm{GHz}})^2 + \left(\frac{\partial S_{1.28\ \mathrm{GHz}}}{\partial \alpha}\right)^2 (\Delta\alpha)^2}, \tag{4.3}$$

where $\Delta S_{1.28\ \mathrm{GHz}} = 0.3$ mJy. We substitute Equation 4.2 into Equation 4.3 and obtain:

$$\Delta S_{943\ \mathrm{MHz}} = \sqrt{\left(\frac{\nu_1}{\nu_2}\right)^{2\alpha} (\Delta S_{1.28\ \mathrm{GHz}})^2 + \left(\frac{\nu_1}{\nu_2}\right)^{2\alpha} \left(S^2_{1.28\ \mathrm{GHz}} \cdot (\Delta\alpha)^2 \cdot \ln^2\left(\frac{\nu_1}{\nu_2}\right)\right)}. \tag{4.4}$$

A summary of the physical properties of the diffuse emission is listed in Table 4.1.

The South East peripheral structure is of interest, as it does not have an X-ray counterpart, making its origin somewhat unclear. The spectral index of the periphery structure appears to match the spectral index of the radio halo. This could indicate that the structure is a part of the radio halo, however, given that the spectral index of the radio halo is calculated including the peripheral structure, this may not be the case. Further high-resolution observations of the galaxy cluster that allow the peripheral structure to be imaged separately is necessary to confirm or disprove this.

Given the position of the peripheral structure on the outskirts of the galaxy structure, and its somewhat elongated extension, the morphology of the structure could hint at a possible radio relic (Duchesne et al., 2021). Our data at present does not allow us to distinguish whether the peripheral structure is a radio relic, however, the polarisation information of the galaxy cluster is a helpful tool. Radio relics are generally strongly polarised at $\gtrsim$ 1GHz, whereas radio halos and bridges are not, thus the polarisation information will serve as a guideline. Our observations include polarisation information, as well as a polarisation calibrator source, thus we intend to continue this work with the analysis of the polarisation.

Properties of A 141	
Average Linear Extent (kpc)	918
S_ν (mJy)	10.8 ± 0.3
$P_{1.4}(10^{23}\,W\,Hz^1)$	14.4 ± 2.0

Table 4.1: Properties of the diffuse emission observed in MeerKAT observations. The radio power and the flux density are scaled to 1.4 GHz for common reference with other observations.

4.1 Comparison with similar systems

In other cases of radio bridges at large scales (such as in Botteon et al. (2020), Govoni et al. (2019)), both X-ray subclusters were found to host radio halos, which could imply that radio bridges form as a result of energy from dynamically active regions being dissipated into the ICM (Botteon et al., 2020), and a lack of a radio halo in the Southern subcluster may indicate the there is not enough dynamic activity for a radio bridge to occur.

Despite this, the 9σ and 12σ contour lines show radio emission extending beyond the Northern subcluster and towards the South. The morphology of these contours is reminiscent of the contours in the radio bridge of A1758 (See Figure 1.6, at 53 MHz and 144 MHz).

Additionally, we find the average surface brightness of the volume-filling radio emission in between the X-ray subclusters to be $< I >_{1.28\text{GHz}} = 0.075 \pm 0.1$ mJy beam^{-1} (0.23 μJy arcsec^{-2}). We compare this to the average surface brightness in A399-401, where the surface brightness is reported to be very low, $< I >_{140\text{MHz}} = 2.75 \pm 0.08$ mJy beam^{-1}, by scaling our average surface brightness as,

$$< I' >_{140\text{MHz}} = < I >_{1.28\text{GHz}} \left(\frac{140\text{MHz}}{1.28\text{GHz}}\right)^{\alpha}. \tag{4.5}$$

We assume a spectral index $\alpha = -1.5$, as constrained in Nunhokee et al. (2023), and find $< I' >_{140\text{MHz}} = 2.08$ mJy beam^{-1}. This falls within 1σ of the average surface brightness of the A399-401 radio bridge, indicating that the surface brightness of the bridge-like structure in A 141 is compatible with that of the radio bridge surface brightness in A399-401. A key finding

in previous studies of radio bridges is a low surface brightness throughout the bridge. This is clearly exhibited in the bridge-like structure of A 141.

Govoni et al. (2019) shows simulations that suggest that the radio bridge emission in A399-401 can be produced by weak-shocks re-accelerating relativistic particles, i.e. via the Fermi I mechanism. However, Brunetti & Vazza (2020) shows that Fermi II (turbulent-induced) re-acceleration mechanisms generate steep spectrum and volume-filling synchrotron emission in the form of giant radio halos and argues that this mechanism is responsible for extended radio bridges.

Nunhokee et al. (2023) constrains the spectral index of A399-401 to be steep, and states that such a steep spectral index cannot be easily explained by the Fermi I mechanism; thus, a steep spectral index favours the Fermi II mechanism. The spectral index of A1758 is also constrained to be steep, thus favouring the Fermi II mechanism. In this thesis, we find that the spectral index of A 141 is flatter than these cases, thus, this result does not fit the currently proposed re-acceleration mechanism. This does not inherently favour the Fermi I mechanism, but rather indicates that future studies should focus on other possible re-acceleration mechanisms that would explain the flatter spectral index.

The radio bridge in A399-401 is detected at 144 MHz by Govoni et al. (2019), and again at 140 MHz by Nunhokee et al. (2023), who also report a non-detection of the bridge at 346 MHz. Similarly, the radio bridge in A1758 is observed at 144 MHz, with a hint of emission being observed at 53 MHz by Botteon et al. (2020), who also reports a non-detection at higher frequencies 383 MHz and 1.5 GHz. Conversely, radio emission corresponding to an X-ray radio bridge associated A 141 is detected as low as 88 MHz by Duchesne et al. (2021), and at 1.4 GHz by this thesis. Such an instance is rare, with only one other example of bridge-like detection at GHz scales.

The Shapley supercluster is the first case of diffuse bridge-like emission between a radio halo in Abell 3567 and the galaxy group SC 1329–313, detected at GHz frequencies by Venturi et al. (2022). The radio and X-ray emission from the bridge in the Shapley cluster shows a strong

correspondence with one another, unlike A 141. This makes A 141 truly a unique case. Due to this, we cannot classify the diffuse emission of A 141 definitively as a radio bridge, as it is unlike previous radio bridges, though the bridge-like nature of the clearly extended diffuse emission is indisputable. With further studies of the possible acceleration mechanism of A 141, or perhaps with the identification of more diverse radio bridges, we could further classify the emission of A 141.

CHAPTER 5

Conclusions

In this thesis, we present new MeerKAT images of Abell 141 at 1.28 GHz, at a factor of ~ 2.5 times deeper, and at a higher resolution than the previous study by Duchesne et al. (2021) at 943.5 MHz. We confirm the presence of centrally located diffuse radio emission that extends towards the South and a South-East peripheral radio source with no X-ray counterpart.

Our improved resolution confirms that the radio emission does not precisely follow the X-ray morphology between the two subclusters. Additionally, we note a misplacement between the peak of the radio and X-ray emission in the Northern subcluster and no peak of radio emission corresponding to the Southern X-ray subcluster. We confirm the halo in the Northern subcluster and the absence of a halo in the Southern subcluster. While we do not have sufficient information to classify this source as a radio bridge, we confirm a low-surface brightness bridge-like emission between the subcluster pair. Further high-resolution studies at lower frequencies are needed to understand the radio morphology's nature.

We find an integrated flux density of 10.8 ± 0.3mJy at a 3σ significance across the entirety of the diffuse emission. The integrated flux density further confirms a spectral index of -1.06 ± 0.09 as first reported in (Duchesne et al., 2021). The somewhat flat spectrum is not in agreement with the proposed interpretation of the acceleration mechanism, involving turbulent induced acceleration, and instead hints towards a different reacceleration mechanism. Additionally, this study confirms the power-law relation of the spectral index.

Abell 141 is the second galaxy cluster to host large-scale radio emission detected at GHz frequencies. The first case and the only other is the Shapley supercluster, which has a strong correlation between radio and X-ray morphology. The misplacement between the radio and X-ray emission in Abell 141 makes it a unique case.

Future work will entail polarisation calibration and imaging, with our polarisation data. The polarisation information will give an indication of the origin of the South East peripheral structure, which can potentially be a radio relic. It can also help extract further information about magnetic fields within the cluster.

Low frequency observations have been key in previous studies of radio bridges, i.e. LOFAR observations in the cases of A 399-A 401 and A 1758. Further low-frequency studies at a higher resolution can be conducted with low-frequency radio telescopes such as the MWA, or GMRT. Such studies will better the understanding of radio morphology in A 141, and aid in the investigation of particle acceleration on large scales.

Bibliography

Ade, P., Aghanim, N., Arnaud, M., et al. 2016, Astronomy & Astrophysics, 594, A27

Akamatsu, H., Fujita, Y., Akahori, T., et al. 2017, in The X-ray Universe 2017, ed. J.-U. Ness & S. Migliari, 30

Balboni, M., Bonafede, A., Bernardi, G., et al. 2023, Astronomy & Astrophysics, 679, A107

Bonafede, A., Intema, H. T., Bruggen, M., et al. 2014, Monthly Notices of the Royal Astronomical Society, 444, L44

Bonjean, V., Aghanim, N., Salomé, P., Douspis, M., & Beelen, A. 2018, Astronomy & Astrophysics, 609, A49

Booth, R. S., de Blok, W. J. G., Jonas, J. L., & Fanaroff, B. 2009, arXiv e-prints, arXiv:0910.2935

Botteon, A., Shimwell, T., Bonafede, A., et al. 2018, Monthly Notices of the Royal Astronomical Society, 478, 885

Botteon, A., Van Weeren, R., Brunetti, G., et al. 2020, Monthly Notices of the Royal Astronomical Society: Letters, 499, L11

Briggs, D. S. 1995, Ph. D. Thesis

Brogan, C. L., Hunter, T. R., & Fomalont, E. B. 2018, Advanced Gain Calibration Techniques in Radio Interferometry, arXiv:1805.05266

Brown, S., & Rudnick, L. 2011, Monthly Notices of the Royal Astronomical Society, 412, 2

Brunetti, G. 2004, Journal of The Korean Astronomical Society, 37, 493

Brunetti, G., & Jones, T. W. 2014, International Journal of Modern Physics D, 23, 1430007

Brunetti, G., & Vazza, F. 2020, Physical Review Letters, 124, 051101

Caglar, T. 2018, Monthly Notices of the Royal Astronomical Society, 475, 2870

Cassano, R., & Brunetti, G. 2005, Monthly Notices of the Royal Astronomical Society, 357, 1313

Cassano, R., Ettori, S., Brunetti, G., et al. 2013, The Astrophysical Journal, 777, 141

Condon, J. J., & Ransom, S. M. 2016, Essential Radio Astronomy, Vol. 2 (Princeton University Press)

Conway, J. E., Cornwell, T. J., & Wilkinson, P. N. 1990, Monthly Notices of the Royal Astronomical Society, 246, 490

Cuciti, V., Cassano, R., Brunetti, G., et al. 2021, Astronomy & Astrophysics, 647, A51

David, L. P., & Kempner, J. 2004, The Astrophysical Journal, 613, 831

Di Gennaro, G., van Weeren, R., Cassano, R., et al. 2021, Astronomy & Astrophysics, 654, A166

Duchesne, S., Johnston-Hollitt, M., & Wilber, A. 2021, Publications of the Astronomical Society of Australia, 38

Duchesne, S. W., Johnston-Hollitt, M., Offringa, A. R., et al. 2021, , 38, e010

Fabian, A., Peres, C., & White, D. 1997, Monthly Notices of the Royal Astronomical Society, 285, L35

Feretti, L., Giovannini, G., Govoni, F., & Murgia, M. 2012, The Astronomy and Astrophysics Review, 20, 1

Forman, W., & Jones, C. 1982, Annual Review of Astronomy and Astrophysics, 20, 547

Fujita, Y., Koyama, K., Tsuru, T., & Matsumoto, H. 1996, Publications of the Astronomical Society of Japan, 48, 191

Fujita, Y., Tawa, N., Hayashida, K., et al. 2008, Publications of the Astronomical Society of Japan, 60, S343

Gendron-Marsolais, M., Hlavacek-Larrondo, J., Weeren, R., et al. 2017, doi:10.17863/CAM.23064

Geyer, M., Girard, J., Grobler, T., et al. 2016, Fundamentals of Radio Interferometry

Giacintucci, S., Markevitch, M., Cassano, R., et al. 2017, The Astrophysical Journal, 841, doi:10.3847/1538-4357/aa7069

Giovannini, G., Tordi, M., & Feretti, L. 1999, New Astronomy, 4, 141

Giovannini, G., Cau, M., Bonafede, A., et al. 2020, Astronomy & Astrophysics, 640, A108

Govoni, F., Orrù, E., Bonafede, A., et al. 2019, Science, 364, 981

Hamaker, J., Bregman, J., & Sault, R. 1996, Astronomy and Astrophysics Supplement Series, 117, 137

Hincks, A. D., Radiconi, F., Romero, C., et al. 2022, Monthly Notices of the Royal Astronomical Society, 510, 3335

Hoeft, M., & Brüggen, M. 2007, Monthly Notices of the Royal Astronomical Society, 375, 77

Hoffman, F. 1997, An Introduction to Fourier Theory, Vol. 2

Högbom, J. A. 1974, Astronomy & Astrophysicss, 15, 417

Hugo, B. V., Perkins, S., Merry, B., Mauch, T., & Smirnov, O. M. 2022, arXiv:2206.09179

Jonas, J., & MeerKAT Team. 2016, in MeerKAT Science: On the Pathway to the SKA, 1

Jones, R. C. 1942, Journal of the Optical Society of America, 32, 486

Józsa, G. I. G., White, S. V., Thorat, K., et al. 2020, in Astronomical Society of the Pacific Conference Series, Vol. 527, Astronomical Data Analysis Software and Systems XXIX, ed. R. Pizzo, E. R. Deul, J. D. Mol, J. de Plaa, & H. Verkouter, 635

Kenyon, J. S., Smirnov, O. M., Grobler, T. L., & Perkins, S. J. 2018, Monthly Notices of the Royal Astronomical Society, 478, 2399

Knowles, K., Cotton, W., Rudnick, L., et al. 2022, Astronomy & Astrophysics, 657, A56

Kravtsov, A. V., & Borgani, S. 2012, Annual Review of Astronomy and Astrophysics, 50, 353

Lockman, F. J. 1998, Advanced Technology MMW, Radio, and Terahertz Telescopes, 3357, 656

Loi, F., Murgia, M., Govoni, F., et al. 2017, Monthly Notices of the Royal Astronomical Society, 472, 3605

Markevitch, M., Forman, W. R., Sarazin, C. L., & Vikhlinin, A. 1998, The Astrophysical Journal, 503, 77

Mazzotta, P., & Giacintucci, S. 2008, The Astrophysical Journal, 675, L9

McMullin, J. P., Waters, B., Schiebel, D., Young, W., & Golap, K. 2007, in Astronomical Society of the Pacific Conference Series, Vol. 376, Astronomical Data Analysis Software and Systems XVI, ed. R. A. Shaw, F. Hill, & D. J. Bell, 127

Molnar, S. M. 2016, Frontiers in Astronomy and Space Sciences, 2, 7

Murgia, M., Govoni, F., Feretti, L., & Giovannini, G. 2010, Astronomy & Astrophysics, 509, A86

Nan, R., Li, D., Jin, C., et al. 2011, International Journal of Modern Physics D, 20, 989

Nunhokee, C. D., Bernardi, G., Manti, S., et al. 2023, Monthly Notices of the Royal Astronomical Society, 522, 4421

Offringa, A. R., McKinley, B., Hurley-Walker, et al. 2014, Monthly Notices of the Royal Astronomical Society, 444, 606

Parekh, V., Van Der Heyden, K., Ferrari, C., Angus, G., & Holwerda, B. 2015, Astronomy & Astrophysics, 575, A127

Pignataro, G. V., Bonafede, A., Bernardi, G., et al. 2023, arXiv e-prints, arXiv:2311.09287

Planck Collaboration, Aghanim, N., Akrami, Y., et al. 2020, Astronomy & Astrophysics, 641, A6

Ramaila, A. J., Smirnov, O., & Heywood, I. 2023, breizorro: Image masking tool, Astrophysics Source Code Library, record ascl:2305.009, ascl:2305.009

Rieger, F. M., Bosch-Ramon, V., & Duffy, P. 2007, in The Multi-Messenger Approach to High-Energy Gamma-Ray Sources, Springer, 119–125

Riess, A. G., Filippenko, A. V., Challis, P., et al. 1998, The astronomical journal, 116, 1009

Rizza, E., Burns, J., Ledlow, M., et al. 1998, Monthly Notices of the Royal Astronomical Society, 301, 328

Roettiger, K., Stone, J. M., & Burns, J. O. 1999, The Astrophysical Journal, 518, 594

Sarazin, C. L. 1986, Reviews of Modern Physics, 58, 1

Schwab, F. R. 1984, Astronomical Journal, 89, 1076

Shimwell, T. W., Brown, S., Feain, I. J., et al. 2014, Monthly Notices of the Royal Astronomical Society, 440, 2901

Smirnov, O. M. 2011, Astronomy & Astrophysics, 527, A106

Struble, M. F., & Rood, H. J. 1999, The Astrophysical Journal Supplement Series, 125, 35

Sunyaev, R. A., & Zeldovich, Y. B. 1970, Astrophysics and Space Science, 9, 368

Thompson, A. R., Moran, J. M., & Swenson, G. W. 2017a, Interferometry and synthesis in radio astronomy (Springer Nature)

Thompson, A. R., Moran, J. M., Swenson Jr, G. W., et al. 2017b, Interferometry and Synthesis in Radio Astronomy, 725

Vacca, V., Govoni, F., Murgia, M., et al. 2022, Monthly Notices of the Royal Astronomical Society, 514, 4969

Van Weeren, R., de Gasperin, F., Akamatsu, H., et al. 2019, Space Science Reviews, 215, 1

Vazza, F., Brüggen, M., van Weeren, R., et al. 2012, Monthly Notices of the Royal Astronomical Society, 421, 1868

Vazza, F., Ettori, S., Roncarelli, M., et al. 2019, Astronomy & Astrophysics, 627, A5

Venturi, T., Giacintucci, S., Dallacasa, D., et al. 2008, Astronomy & Astrophysics, 484, 327

Venturi, T., Giacintucci, S., Merluzzi, P., et al. 2022, Astronomy amp; Astrophysics, 660, A81

Wittor, D., Domínguez-Fernández, P., Vazza, F., & Brüggen, M. 2019, A Song of Shocks and Dynamo: Numerical Studies of a Galaxy Cluster Merger in the HIMAG Project, arXiv:1909.10792

Young, T. 1807, A Course of Lectures on Natural Philosophy and the Mechanical Arts: in Two Volumes, Vol. 2 (Johnson)